

SURFACE INTEGRITY AND ENERGY CONSUMPTION IN MACHINING OF INCONEL
718 PRODUCED BY SELECTIVE LASER MELTING

by

DANIEL BROWN

YUEBIN GUO, COMMITTEE CHAIR
J. BRIAN JORDON
MARK L. WEAVER

A THESIS

Submitted in partial fulfillment of the requirements
for the degree of Master of Science in the
Department of Mechanical Engineering
in the Graduate School of
The University of Alabama

TUSCALOOSA, ALABAMA

2017

Copyright Daniel Brown 2017
ALL RIGHTS RESERVED

ABSTRACT

The development of additive manufacturing (AM) in the past decade has brought along with it a number of new opportunities and challenges when it comes to how parts are manufactured. While this development represents an increase in the capabilities and performance of the AM parts, much work and research still needs to be done in order to ascertain how to avoid the limitations that plague AM such as low dimensional accuracy, high surface roughness, and large tensile residual stress. Ongoing efforts to improve part quality through process optimization of parameters such as scan speed and laser power, post heat treatment, or machining, are currently being pursued to mitigate these limitations, and it is likely that the fabrication of a functional part lies within the use of all of these efforts.

Little study has been done to characterize surface integrity of an as-SLM part followed by milling (e.g., hybrid SLM-milling). In this paper, surface integrity including surface roughness, microstructure, and microhardness have been characterized for the IN718 samples processed by the hybrid process. It has been found that surface integrity can be significantly improved by the hybrid SLM-milling route.

To investigate the machinability of the deposited materials, energy consumption was collected and analyzed in terms of specific energy between dry and flood milling of as-SLM IN718, dry-milling of conventional IN718, and flood-milling of conventional IN718. Energy consumption was the lowest for both flood milling cases compared to the dry milling case, and the lowest for both as-SLM cases in comparison to the conventionally produced cases.

DEDICATION

This thesis is dedicated to everyone who helped me and guided me through the graduate study and research. In particular, it is dedicated to my parents, my sister, the Laukien family, and my fellow student Connor Whatley.

LIST OF ABBREVIATIONS AND SYMBOLS

AM	Additive Manufacturing
RP	Rapid Prototyping
SLS	Selective Laser Sintering
SLM	Selective Laser Melting
EBM	Electron Beam Melting
HIP	Hot Isostatic Pressing
v	Cutting speed
f_z	Feed per tooth
α_c	Radial Depth of Cut
α_p	Axial Depth of Cut
MRR	Material Removal Rate
U_{nc}	Net cutting specific energy
U_s	Spindle specific energy
U_M	Machine specific energy

ACKNOWLEDGEMENTS

I would like to express my gratitude first to my graduate advisor, Dr. Yuebin Guo, for his extensive help and guidance throughout the course of my graduate education. I would like to thank my committee members, Dr. Mark Weaver and Dr. Brian Jordon, for their proofreading the thesis and support to my research. Thanks also go to my fellow graduate student Mr. Chao Li for assisting, teaching, and directing me as I progressed through this research process. Finally, I would like to thank my fellow graduate student Mr. Ziye Liu for his assistance in conducting the machining experiment and energy consumption analysis.

CONTENTS

ABSTRACT	ii
DEDICATION	iii
LIST OF ABBREVIATIONS AND SYMBOLS	iv
ACKNOWLEDGEMENTS	v
LIST OF TABLES	ix
LIST OF FIGURES	x
CHAPTER 1 LITERATURE REVIEW	1
1.1 Review of Additive Manufacturing	1
1.1.1 Additive Manufacturing of Metal Parts	1
1.1.2 Process Mechanisms	2
1.1.2.1 Powder Bed Fusion.....	2
1.1.2.2 Direct Energy Deposition	3
1.1.3 Applications and Requirements of AM Metal Parts	4
1.1.3.1 Applications in the Medical Industry	5
1.1.3.2 Applications in the Aerospace Industry	5
1.1.3.3 Applications in the Automotive Industry	6
1.1.4 Applied Materials	6
1.1.5 Critical Issues for LAMed Metal Parts	7
1.1.5.1 Dimensional Accuracy	7

1.1.5.2 Surface Integrity	9
1.1.5.3 Coarse Microstructure	11
1.1.5.4 Voids/Porosity	13
1.1.5.5 Mechanical Properties	14
1.1.5.6 Balling Effect.....	16
1.1.5.7 Tensile Residual Stress.....	18
1.1.5.8 Influence of Scanning Strategy	24
1.1.5.9 Fatigue Performance.....	27
1.1.5.10 Wear Performance.....	33
1.2 Review of Machining of LAM Parts	35
1.2.1 Machining Processes	35
1.2.2 Surface Integrity	35
1.2.2.1 Roughness.....	36
1.2.2.2 Hardness	36
1.2.2.3 Residual Stress.....	37
1.3 Summary of Review	40
CHAPTER 2 EFFECTS OF MACHINING ON SURFACE INTEGRITY OF IN718 MADE BY SELECTIVE LASER MELTING	41
2.1 Introduction.....	41
2.2 Experiment.....	43
2.2.1 SLM Experimental Set-Up	43
2.2.2 Milling Experimental Set-Up	46
2.2.3 Mounting Set-Up	47
2.3 Results on Surface Integrity.....	48

2.3.1 Microstructure.....	48
2.3.2 Roughness.....	54
2.3.3 Hardness	58
2.4 Summary.....	63
CHAPTER 3 ENERGY USAGE IN MILLING OF SELECTIVE LASER MELTED IN718	64
3.1 Introduction.....	64
3.2 Experiment.....	65
3.3 Energy Consumption Characteristics	66
3.3.1 Comparison of Flood and Dry Milling	67
3.3.2 Comparison of Milling Conventional and SLMed IN718	71
3.3.2.1 Flood Milling.....	71
3.3.2.2 Dry Milling.....	73
3.4 Summary.....	75
CHAPTER 4 SUMMARY AND FUTURE OUTLOOK	77
REFERENCES	79

LIST OF TABLES

1.1 AM technologies, acronyms, and development years	2
1.2 Selected alloys commercially used in AM.....	7
1.3 Mechanical Properties of Inconel 625	15
1.4 Details of the Sample Batches	30
1.5 Materials and Machines used in Fretting Tests.....	33
2.1 Sample Preparation	45
2.2 Milling Parameters.....	46
2.3 Ra Values from Machined Samples.....	56
3.1 Energy Data of SLMed Samples.....	70
3.2 Energy Data of Flood Milling SLMed and Traditional IN718	72
3.3 Energy Data of Dry Milling SLMed and Traditional IN718	74

LIST OF FIGURES

1.1 Diagram of SLM setup.....	3
1.2 Diagram of LMD Setup	4
1.3 Part Distortions, Residual Stresses, and Crack Formation in SLM	8
1.4 Influence of Process Parameters on Dimensional Deviation.....	8
1.5 Influence of Laser Power and Scanning Speed on Roughness Ra values	10
1.6 Surface Roughness in SLM part	11
1.7 Thermal Profile of a single layer of SLMed Ti-6Al-4V	11
1.8 Images of Columnar grain growth in SLMed Ti-6Al-4V	12
1.9 Examples of voids in SLM Parts	14
1.10 Depiction of Balling Effect.....	16
1.11 Balling Effect Mechanisms.....	17
1.12 Process window for (a) CW operation and (b) pulsed operation.....	18
1.13 Induction of Residual Stresses due to Thermal Gradient.....	19
1.14 Crack Initiation due to Tensile Residual Stresses.....	19
1.15 Influence of the number of layers on the residual stress profile	20
1.16 Influence of material's yield strength on the residual stress profile	21
1.17 Influence of base plate heating	22
1.18 Scanning Strategy (for Figure 16).....	22
1.19 Distortion vs. Initial Platform Temperature.....	23

1.20 Base plate, supports, and part geometry	23
1.21 Scanning Strategies.....	24
1.22 Normal Stresses on the cantilever in the (a) horizontal direction and (b) vertical direction.....	25
1.23 Scanning Strategies used for Comparison	26
1.24 Curvature along X-axis and Y-axis vs. Strategy.....	27
1.25 Tensile Residual Stress Crack Initiation	28
1.26 Samples (static tensile) built in different directions	29
1.27 Fatigue Resistance of batches built at 30°C platform temperature.....	31
1.28 Fatigue Resistance of batches (a) built at 300°C platform temperature and (b) that are peak hardened.....	32
1.29 Surface roughness of samples.....	36
1.30 Hardness depth measurements.....	37
1.31 Residual stresses on surface.....	38
1.32 Residual stress profiles of SLM-samples with (a) horizontal and (b) vertical layer orientation	38
1.33 Residual Stress Profiles of AISI 52100	39
2.1 SLM schematic	41
2.2 SLM set-up.....	43
2.3 SEM images of Inconel 718 powder particles	44
2.4 Depiction of scanning patterns.....	46
2.5 Plane Orientation for Samples	47
2.6 Sectioning schematic	47
2.7 Mounting schematic.....	48
2.8 YZ-Plane of Sample 4.....	49

2.9 XZ-plane of Sample 5	49
2.10 Balling Effect.....	51
2.11 Balling Effect in XZ-plane of Sample 5	52
2.12 Depth Profile of Void in Sample 5	53
2.13 Balling Effect on XY-plane of Sample 1 Prior to Machining	54
2.14 Surface Topography of Sample 1 Prior to Machining	55
2.15 Surface Topography of Sample 1 After Machining.....	56
2.16 Hardness Test on YZ-plane of Sample 3	59
2.17 Hardness Test on XZ-plane of Sample 5	60
2.18 Hardness of Part-Substrate Interface on XZ-plane of Sample 5	61
2.19 Hardness Profile of Samples 3, 4, and 5	62
3.1 Sample dimensions	66
3.2 Spindle Energy and Power Consumption in Flood Milling of SLMed IN718.....	68
3.3 Spindle Energy and Power Consumption in Dry Milling of SLMed IN718	69
3.4 Spindle Energy and Power Consumption in Flood Milling of Traditional IN718.....	71
3.5 Porosity in SLM produced Samples	73
3.6 Spindle Energy and Power Consumption in Dry Milling of Traditional IN718.....	74

CHAPTER 1

LITERATURE REVIEW

1.1 Review of Additive Manufacturing

1.1.1 Additive Manufacturing of Metal Parts

The term additive manufacturing (AM) denotes a process of part fabrication that builds objects through the addition of material, in contrast to subtractive methods. The rise of AM began with the successful development and commercialization of the stereolithographic process by 3D systems in 1993 [1]. This process is characterized by curing a liquid resin layer-by-layer with a laser system through photo-polymerization. While the ease of use and development of such a system was highly important for the rise of Rapid Prototyping (RP), there neglected to be a process capable of building functional metallic parts that would be comparable in surface finish, strength, and fatigue life to those made by conventional processes. This is a problem that continues today, as AM processes are typically plagued by a rough surface finish and diminished fatigue life when compared to conventional manufacturing techniques. Table 1.1 details an overview of the developmental years of some of the preliminary AM techniques.

Table 1.1 AM technologies, acronyms, and development years [2]

Name	Acronym	Development years
Stereolithography	SLA	1986 - 1988
Solid Ground Curing († = year of disappearance)	SGC	1986 - 1998 1999†
Laminated Object Manufacturing	LOM	1985 - 1991
Fused Deposition Modelling	FDM	1988 - 1991
Selective Laser Sintering	SLS	1987 - 1992
3D Printing (Drop on Bed)	3DP	1985 - 1997

As the development of additive manufacturing techniques as a whole continued to rise, increasing emphasis was placed on developing processes that could create metallic parts. The processes that were developed used two primary mechanisms in order to build a part layer by layer: Powder Bed Fusion and Direct Energy Deposition. While there are many ways that these systems can be classified, the easiest and simplest method is to divide the processes into two groups dependent on the manner of powder deposition.

1.1.2 Process Mechanisms

1.1.2.1 Powder Bed Fusion

Powder Bed Fusion, as its name indicates, represents the group of processes that utilize a thin layer of powder that has been pre-deposited on a surface. This is typically done by using a roller or rake which pushes the powder onto the part base plate. Common processes using this mechanism include Selective Laser Sintering (SLS), Selective Laser Melting (SLM) and Electron Beam Melting (EBM). In the cases of SLS and SLM, a laser is used to either sinter or melt (respectively) the particles together in order to create a layer of the piece. EBM, as its name indicates, utilizes an electron beam to melt the powder together into the desired shape. It also differs from the laser-based methods in that the process must be performed in a vacuum in order

to prevent collisions between the electrons and air or gas molecules [3]. After one layer is complete, the part is lowered by the layer thickness and a fresh powder bed is deposited. Figure 1.1 shows a typical SLM set-up.

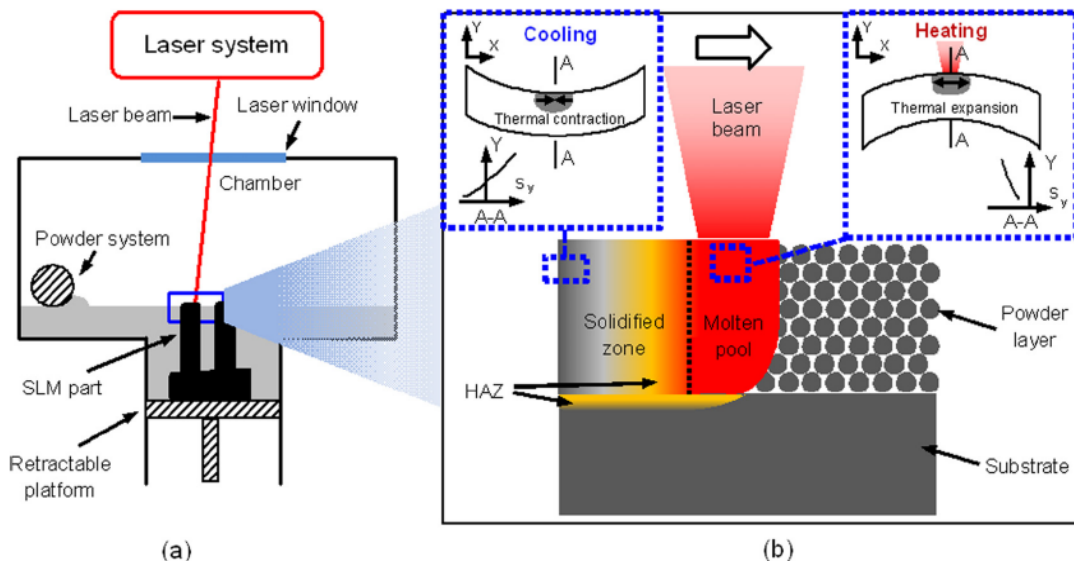


Figure 1.1 Diagram of SLM setup [4]

1.1.2.2 Direct Energy Deposition

Direct Energy Deposition processes differ from Powder Bed Fusion in that the material to be used is deposited as it is melted together and hardened rather than being first pre-deposited, and then sintered/melted in a subsequent step. In these processes, the metal powder or wire is deposited into the laser beam through a nozzle. When used with a laser beam as the energy source, this process can also be called Laser Cladding, and has the added benefit (in comparison to powder bed systems) of being able to be used to repair parts. Equipment of this type either has one of two systems: one with a stationary build part and a moving deposition head, or vice versa

with a moving build part and a stationary deposition head [5]. One such process that utilizes this method is Laser Metal Deposition, depicted in Figure 1.2.

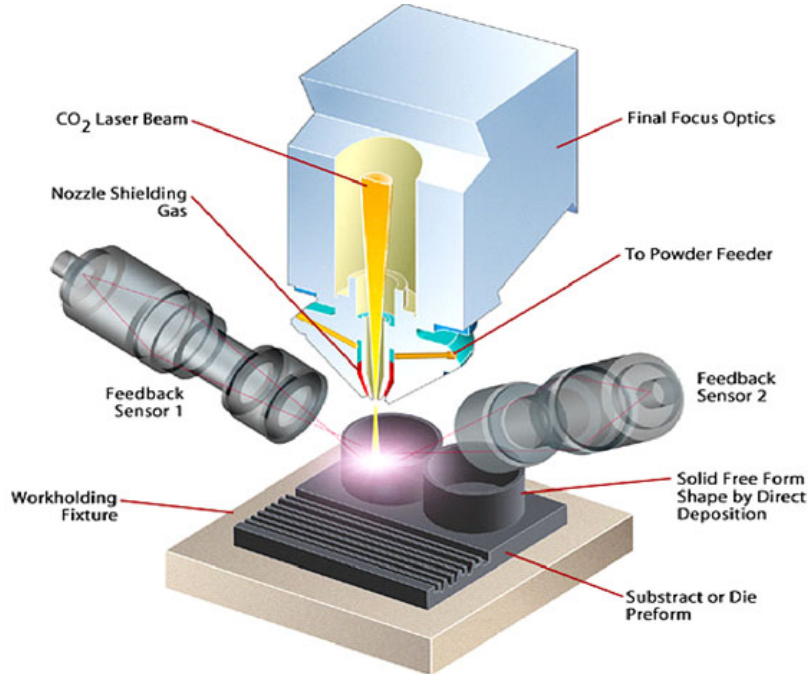


Figure 1.2 Diagram of LMD Setup [6]

Material Extrusion, or wire feed, processes also fall under the category of Direct Energy Deposition in that the material is fed or deposited in the system as it is melted and solidified. This process is identical to the powder fed mentioned above and differs only in the manner of deposition [2]. While many processes make use of a laser, the energy source can also be an electron beam or a plasma arc [7].

1.1.3 Applications and Requirements of AM Metal Parts

Many of the practical applications of AM parts in industry come from the ability to quickly prototype pieces, especially those with complex geometries that would be extremely difficult to machine. Another practical application lies in rapid tooling, the ability to quickly and

efficiently manufacture tools such as molds for use in commercial operations. In essence, any industry driving for shorter lead times, customizable complex parts, and lower material costs will benefit from AM parts, especially as the reliability, strength, and fatigue life of the parts increase.

1.1.3.1 Applications in the Medical Industry

A primary use of AM in the medical industry comes with the ability to quickly and accurately create implants customized to individual needs. These “customized products provide superior comfort and lead to a faster recovery” [9], which makes them an obvious next step in implant technology. Fabricating implants with a rough surface structure promotes integration into the bone and shortens recovery time. Additionally, AM is suited for this kind of demand-based need and is able to produce parts with “material properties superior to traditional manufactured counterparts” [9]. The successful use of AM in the medical industry has the potential to improve the functionality of stents, prosthetics, implants, plates and screws.

1.1.3.2 Applications in the Aerospace Industry

The aerospace industry’s current use of AM is mostly limited to Rapid Prototyping and concept modelling, due to issues with fatigue life and part strength. NASA uses AM to 3D-print pieces for vehicles like their Mars Rover. The flexibility in design and speed of prototyping these pieces allow NASA to save money when creating their test vehicles. The high level of customization for these needs means that money cannot be continuously spent on prototyping complex pieces, making AM a natural primary choice for development [10]. Additionally, the design freedom integral to AM processes allows engineers to create products with more efficient

cooling channels which is otherwise impossible through traditional manufacturing methods. This will allow a greater efficiency and effectiveness in aeronautical systems. Quite famously, GE has already begun to integrate AM parts into its product line. This includes sensor housings and fuel nozzles, with the former being the first AM part to be certified and approved by the FAA [11].

1.1.3.3 Applications in the Automotive Industry

The automotive industry can benefit from AM parts in a similar way as the aerospace industry. The complex geometries which AM is capable of creating allow new designs to be created, resulting in overall product innovation. Essentially, the benefits of AM in the Auto Industry are up to the engineers designing future automobiles. Additionally, the use of AM has the potential to revolutionize the supply chain since AM parts do not require special tooling or any more material than is actually required for the part (as in machining).

1.1.4 Applied Materials

Due to the nature of laser-based AM processes, nearly all metals can be thought of as candidates for use. However, each material may pose large differences in terms of processing difficulty. The mechanics of the melt pool varies from material to material and plays a large role in the characteristics of the final part. Different materials may be more or less susceptible to the balling effect and other surface integrity issues like high roughness. Because of this need for testing and optimization of each powder used, there is currently a limited (albeit rapidly expanding) variety of metal powders that produce high quality parts. Out of those being used, some materials are single material powder such as a pure titanium powder being investigated by Fraunhofer Institute ILT and the Universities of Osaka [12]. Parts with this powder can be

readily made with near full part density, however may be more susceptible to thermal stresses. Figure 1.14 shows such a part made from pure titanium. A crack seen in the bottom left of this figure arises from thermal gradient mechanisms. Additionally, powders are available consisting of alloyed materials. From these, many stainless steels and tool steels are available, as well as a titanium alloy TiAl6V4 which is being heavily tested for medical implants. Table 1.2 presents a number of currently available powders used in AM.

Table 1.2 Selected alloys commercially used in AM processing [7]

Aluminum	Tool Steels	Stainless Steel	Titanium	Super alloys	Refractory
Al-Si-Mg	H13	316 & 316L	Ti-6Al-4V	IN625	MoRe
6061	Cermets	420	ELI Ti	IN718	Ta-W
		347	CP Ti	Stellite	CoCr
		PH 17-4	γ -TiAl		

1.1.5 Critical Issues for LAMed Metal Parts

While the practical uses of Layer Additive Manufactured (LAMed) Parts are widespread and heavily desired in industry, these processes and the parts they create are currently being held back due to a number of critical issues that affect dimension accuracy, surface integrity, and part performance.

1.1.5.1 Dimensional Accuracy

Due to the high thermal gradients at work in LAM processes, a number of key defects can arise. This thermal gradient along with any related plastic behavior leads to a reduction in dimensional accuracy as well as an increase in residual stresses and thermally-induced cracks in the part [13]. Additionally, the use of a larger diameter beam may cause a larger melt pool and

lower dimensional accuracy; a problem Bremen wrote about circumventing through the use of a laser source with a variable focus diameter [14]. A typically used method for assuring final part accuracy is post-processing such as machining. Figure 1.3 shows the results of these behaviors in SLMed parts.

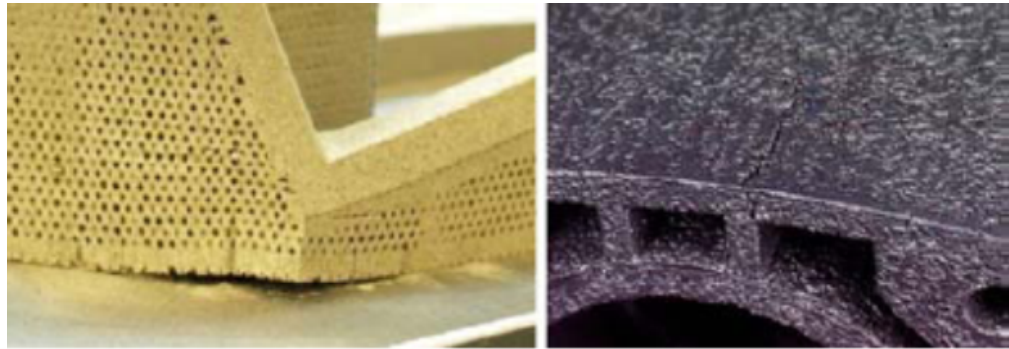


Figure 1.3 Part Distortions, Residual Stresses, and Crack Formation in SLM [13]

Additionally, process parameters such as scanning speed and laser power can have a notable effect on dimensional deviation. Figure 1.4 details the effects of these parameters on dimensional deviation.

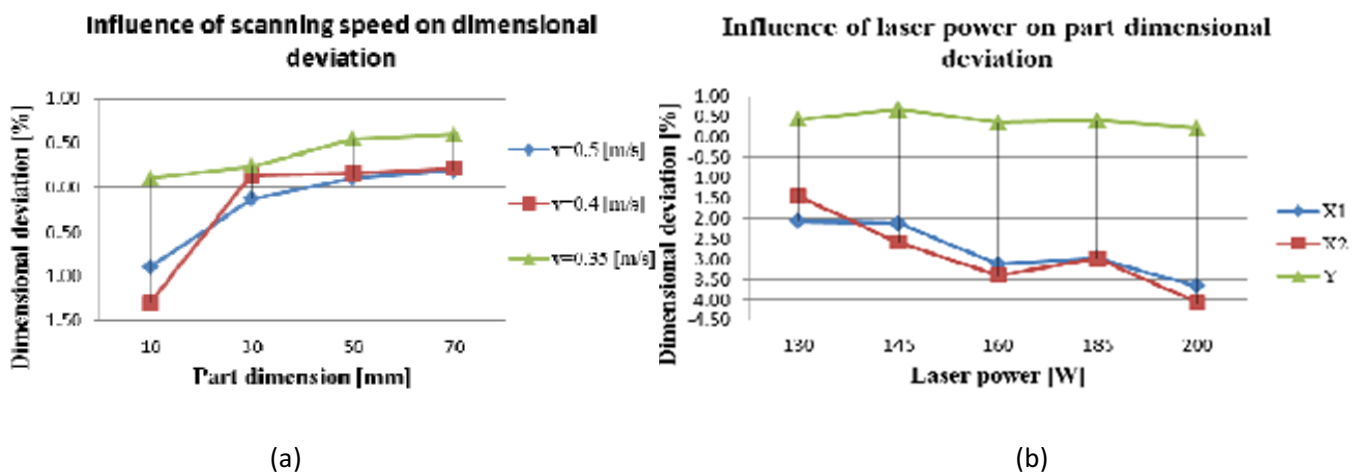


Figure 1.4 Influence of Process Parameters on Dimensional Deviation [15]

Figure 1.4a graphically shows the relationship between scanning speed and dimensional deviation. An additional factor that Prem found to be an influence on the final dimensional deviation of the part is the part size, depicted on the x-axis in Figure 1.4a. This data shows that for smaller parts (dimensions less than 10 mm), a low scanning speed (in this case 0.35 m/s) results in high accuracy. Conversely, with parts larger than 10 mm, the lower scanning speed causes a larger melt pool to grow which will attract excess powder from the surrounding material.

Figure 1.4b shows the relationship between the laser power and dimensional deviation. The red and blue lines detail X1 and X2, which Prem uses to clarify the transverse and longitudinal axis parallel to the build layers. These axis are typically denoted as X and Y in engineering literature. The green line details Y, which Prem uses to clarify the vertical axis; typically referred to as the Z-axis in engineering literature. From this figure, it is evident that an increase in laser power results in increasing dimensional deviations in the horizontal axes. This logically corresponds again with the larger melt pool that will result from this increase in laser power, causing excess powder to be melted into the part structure.

1.1.5.2 Surface Integrity

LAMed parts are susceptible to high surface roughness as a result of “surface defects originating from melt pool dynamics” [14]. Roughness is found to decrease with higher laser power and lower scanning speed, as these two factors allow for a more complete and thorough melting of the powder bed. However, herein lies the tradeoff between dimensional accuracy and surface roughness. As the laser power increases and the scanning speed decreases, the size of the

melt pool increases as a result, meaning higher laser power and lower scan speeds will result in a less dimensionally-accurate part [15].

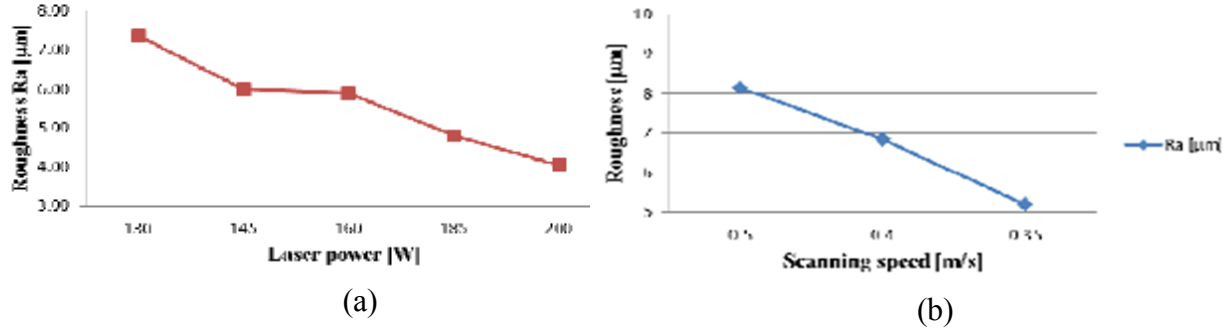


Figure 1.5 Influence of Laser Power and Scanning Speed on Roughness Ra values [15]

Figure 1.5a shows the relationship between laser power in Watts and resultant Ra values in a SLMed part. This shows that increasing laser power correlates with decreasing Ra values. This is expected as the higher laser power will typically result in a more thorough melting of the powder bed.

Figure 1.5b details a similarly expected relationship between roughness and scanning speed. In this graph, the x-axis represents the scanning speed in decreasing intervals. The downward slope of this line shows that roughness values decrease as scanning speed decreases, meaning their relationship is direct. Again, this is logical as a slower scanning speed allows a higher amount of energy to be transferred from the laser into the melt pool, allowing a more complete melting of the powder. Figure 1.6 shows what the typical surface of a SLM part looks like under 50x magnification. Roughness like this serves to greatly reduce the fatigue life of a SLM-produced part as each of the sharp angles can act as an initiation point for crack growth.

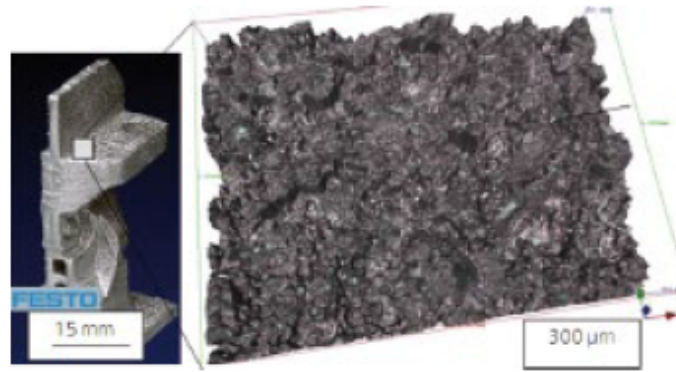


Figure 1.6 Surface Roughness in SLM part [14]

1.1.5.3 Coarse Microstructure

The layer-based AM process experiences major and constant temperature changes that greatly affect the microstructure of the final part. The constant heating and cooling with each laser pass results in the material experiencing many phase transformations. Figure 1.7 shows a complex thermal profile based on a single layer of Ti-6Al-4V [16]. In this figure, it can be seen that the material experiences two transformations between liquid and solid phases and two transformations between alpha and beta phases.

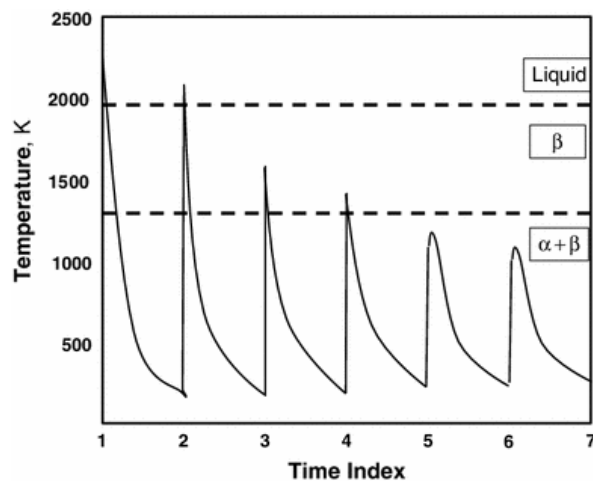


Figure 1.7 Thermal Profile of a single layer of Ti-6Al-4V [16]

Due to the nature of a moving laser winding across the part surface, the temperature deposition is largely directionally-dependent. This is dependent on the scanning strategy used, which is talked about later, however linear passes by the energy source frequently create columnar microstructures with anisotropic properties. By varying laser direction, or through the use of laser pulses, a mixed or equiaxed structure can also be achieved, however there may still be a directional component to the grain growth resulting in varying strengths and fatigue performance on a part when loaded in different directions. Figure 1.8 shows this columnar behavior in parts produced by the ARL Penn State's laser-based direct energy deposition system (a and b) and NASA's electron-based wire fed system (c) [7].



Figure 1.8 Images of Columnar grain growth in Ti-6Al-4V: (a) laser powder blown single bead wide, (b) laser powder blown three bead wide, and (c) electron beam wire three bead wide [7]

The direction of these grains is seen to be perpendicular to the build layer, and represents a further complexity not typically seen in conventional manufacturing techniques. These extreme microstructure phase changes can also cause voids and porosity that may serve as points for crack initiation.

1.1.5.4 Voids/Porosity

In a similar manner as rough surface finishes, LAMed parts are susceptible to internal voids and porosity as well. Figure 1.9 shows three examples of how voids can develop in LAMed parts. The voids present in Figure 1.9a formed due to residual gas content in the powders. This residual gas began as dissolved elements (such as Hydrogen) in the powder material. This effect however can be reduced by up to 50% by drying the powder before use and by up to 90% by using a lower laser power in order to induce a drying effect [17]. Figure 1.9b shows the voids resulting from a lack of fusion between layer boundaries. This type of void can be reduced or eliminated by “increasing laser power, lowering traverse speed, or using thinner layers” in order to promote fusion [17]. The types of voids shown in Figure 1.9c depend on the balling effect which will be discussed further in the next section. Essentially, when a track of molten powder possesses a high viscosity or wetting angle, it can easily form into a ball (noted with arrows in Figure 1.9c) in order to minimize its surface energy. As more of the balls form the surface becomes notably rougher and pores begin to form inside the part [18].

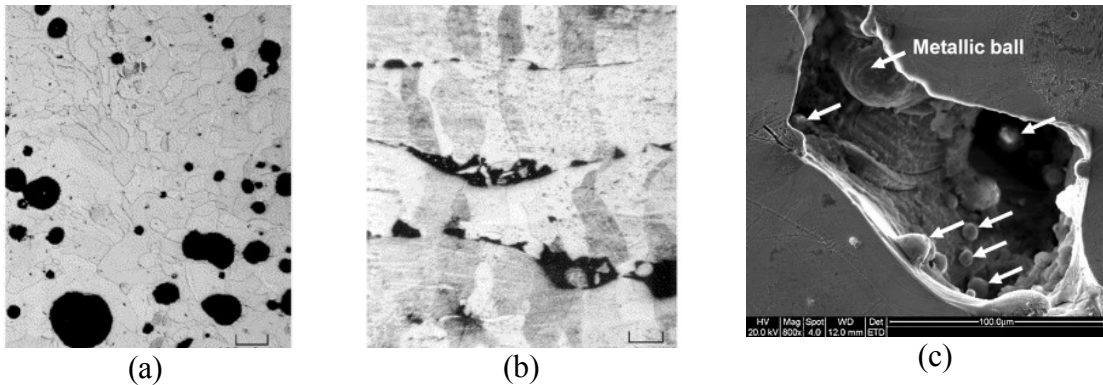


Figure 1.9 Examples of voids in SLM Parts [17, 18]

1.1.5.5 Mechanical Properties

Mechanical Properties of materials made through AM processes are, as can be readily assumed, mostly dependent on the powder material. Following this, the properties are next dependent on the microstructure and process parameters used. As a result of the first factor, this section will focus on a few select materials.

As Ti-6Al-4V is one of the most studied AM materials, this section will focus on its mechanical properties. Kirchner et al. tested this material when fabricated through EBM [19]. The exact chemical composition of the powder tested was 6.4% Al, 4.2% V, and 0.2% Fe. The final products were also heat treated between 650°C and 1050°C. They consisted of hot isostatic pressing (HIP) treatments with maximum pressures of 200 MPa. The length of heat treatment varied from 0.2 to 2 hours. The findings of tensile experiments found Young's moduli to be similar to the wrought product. All of the different heat treatments yielded similar yield strength (YS) and ultimate tensile strength (UTS), with some variations. The final products were found to have a UTS of around 1000 MPa when optimized. The combination of HIP and thermal treatments were also found to significantly improve fatigue life, allowing AM Ti-6A-4V to almost match performance of conventionally manufactured material. AMS 4999 lists the as-built

properties as having slightly lower UTS than 896 MPa (in the build/deposition direction) and 841 MPa (normal to the build direction) reported by Kirchner. This also lists the elongation as 4% and the yield strength as 800 MPa in the build direction and 745 MPa in the directions normal to the build direction. After HIP treatments, the YS and UTS were found to be comparable to those by Kirchner, with maximum yield strengths of 946 MPa and maximum ultimate strengths of 1010 MPa (both in the z-direction, normal to the x-direction, i.e., build direction) [19].

Some of the most important materials for use in AM in the aerospace industry are Nickel-based Superalloys, due to their ability to withstand high operating temperatures. The HIP treatments were performed at temperatures of 1393 K and pressure of 100 MPa for 4 hours. As discussed above is typical, the as-fabricated EBM featured columnar grains which broke down and recrystallized during the HIP treatment. This increased the ductility significantly, marginally increased the tensile strength, and decreased the yield strength. Data comparing Wrought annealed, EBM-manufactured, EBM and HIP treated, and wrought (cold-worked) are listed in Table 1.3.

Table 1.3 Mechanical Properties of Inconel 625 [7]

Process	Yield Strength (YS), MPa	Tensile Strength (UTS), MPa	% Elongation
Wrought (annealed)	450	890	44
As-fabricated EBM	410	750	44
EBM + HIP	330	770	69
Wrought (cold worked)	1,100	---	18

1.1.5.6 The Balling Effect

The balling effect, depicted in Figure 1.10, occurs when the molten material does not wet the underlying substrate due to surface tension [12]. This effect combined with the surface tension of the liquid, causes the material to spheroidise, resulting in a rough surface with decreased density.

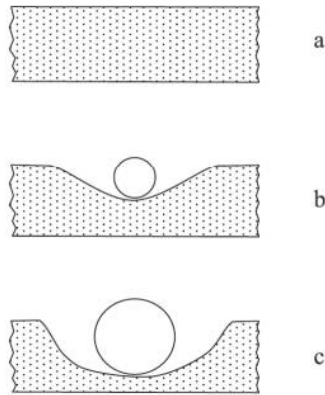


Figure 1.10 Depiction of Balling Effect [20]

The mechanisms behind the formation of these balls are dependent on the angle of interaction between the surface and the molten liquid track. It is appropriate to approximate the molten track as a half cylinder, as shown in Figure 1.11. The balling effect occurs when the total surface of the molten pool becomes larger than that of a sphere with the same volume. The capillary force is able to form this sphere in order to minimize its surface energy. Thus, in order to combat this effect, laser parameters should be optimized in order to minimize the length to diameter ratio of the molten pool [12].

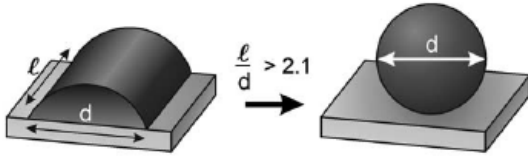


Figure 1.11 Balling Effect Mechanisms [12]

Kruth determined a process window for continuous wave and pulsed laser operations that would provide a smooth surface finish and microstructure. Figure 1.12a depicts the process window for continuous wavelength laser operation, while Figure 1.12b depicts the process for pulsed operation. In general, these figures show that high laser power and high scan speeds result in less balling because the melt pool quickly solidifies behind the laser, keeping the length of the molten track short. However, it should be noted that other studies have shown the opposite effect of no balling at very low scan speeds and low laser power. A reasoning for this that would coincide with the length-diameter relationship of the balling effect shown in Figure 1.11 is that a low scan speed results in a wider scan track (higher track diameter) due to heat conduction [12]. When looking at pulsed operation, it was found that higher peak powers resulted in a better interlayer connection (avoiding voids such as those found in Figure 1.9b) as well as a higher melt pool temperature which has a positive effect on the balling phenomenon [12].

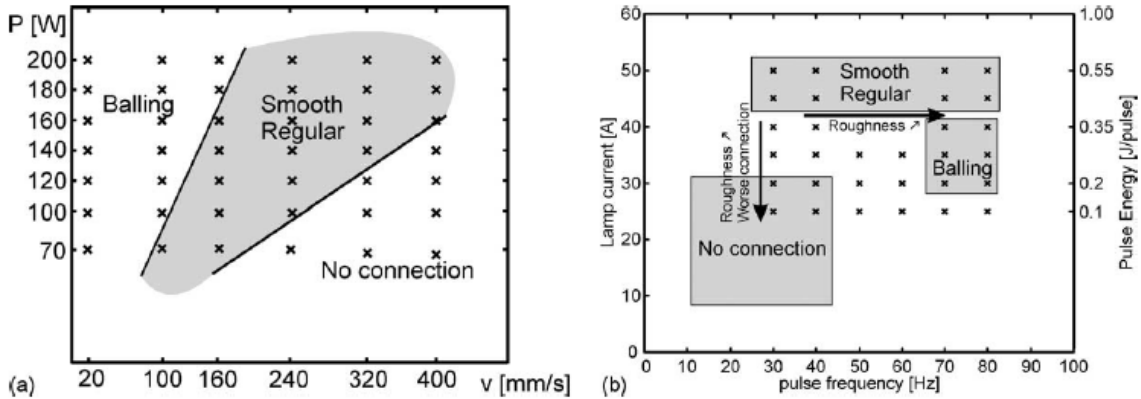


Figure 1.12. Process window for eliminating balling (a) CW operation; (b) pulsed operation [12]

Additionally, wetting between liquid metals and oxide films is nonexistent, so it is highly important to avoid oxidation during the SLM build process. This can be achieved through remelting of the underlying layer in order to remove any contaminants and provide a clean interface at the atomic level [12]. Finally, wetting can be improved by adding certain alloying elements.

1.1.5.7 Tensile Residual Stresses

One of the most researched topics in regards to LAMed parts is the creation of residual stresses as a result of the high thermal gradients. Since lower layers are cooling while upper layers are being heated to their melting point, there exists a large disparity in layer temperatures. This disparity means that one layer is contracting (as it cools) and another is expanding (as it melts) and when these layers solidify together, the stress from expanding and contracting away from each other is contained and locked into the material, ultimately reducing part strength and performance. The creation of these residual stresses is shown in Figure 1.13. As the laser heats the part, the upper layer expands creating a thermal strain. After the layer passes, the part

solidifies and cools rapidly, causing an opposite strain to be placed on the upper layer of the part, creating a tensile residual stress at that point.

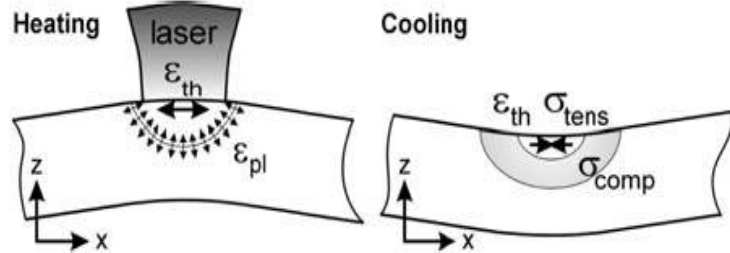


Figure 1.13 Induction of Residual Stresses due to Thermal Gradient [21]

Figure 1.14 shows the effect that these residual stresses can have on a part. The part is made of titanium and produced through SLM. The resulting density is almost 100%, however a large crack is shown in the bottom left corner. Cracks like this need to be reduced in the future as they dramatically reduce part fatigue life to the point where the use of such a part is not feasible [22].

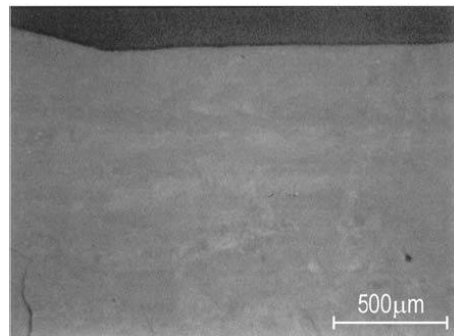


Figure 1.14 Crack Initiation due to Tensile Residual Stresses [22]

A number of process parameters can have an effect on the residual stresses. Figure 1.15 shows the relationship between the number of layers and the residual stress profile. Before

removal of the part from the base plate, the part stress is equivalent to the yield strength at the upper layer [21]. As the number of layers increases however, compressive stresses are imparted at the bottom of the part. It is possible that these stresses could become large enough to induce plastic deformation in the base plate. After the part is removed from the base plate, the stress profile becomes mostly symmetrical, with tensile stresses on the top and bottom surface and an area of compressive stresses in the middle [21]. In Figure 1.15 it is shown that as the number of layers increases (shown by thickness of the part in 50 micron increments) the resulting tensile stresses at the upper surface and compressive stresses in the subsurface increases in magnitude as well. It should be noted that these stresses were recorded in a SLM produced part.

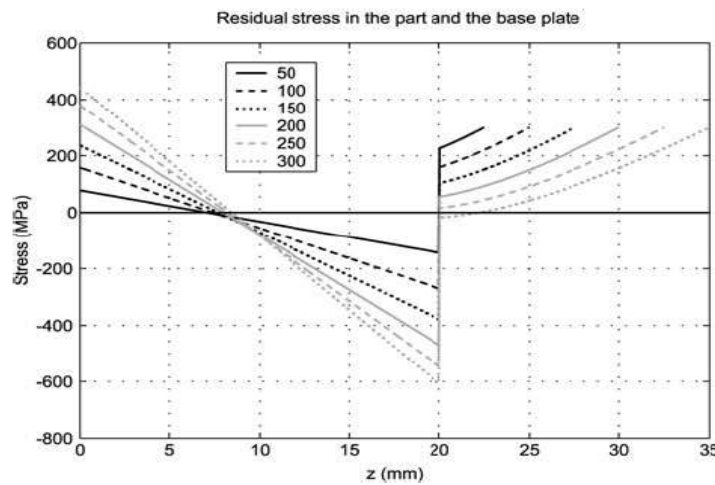


Figure 1.15 Influence of the number of layers on the residual stress profile [21]

Figure 1.16 shows the influence of the material's yield strength on the residual stress profile. This shows that as the yield strength of a material increases, the resultant residual stresses increase as well. This does not necessarily result in an increased likelihood of part deformation or crack initiation however, as the higher yield strength of the part may also allow it to combat these effects.

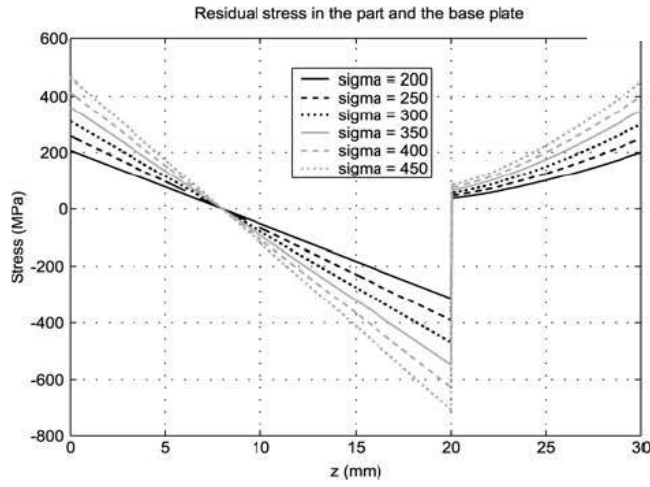


Figure 1.16 Influence of material's yield strength on the residual stress profile [21]

There are a number of ways to combat these residual stresses including preheating of the part (through chamber or base plate heating) and scanning strategy optimization. Additionally, the residual stress profile can be improved through post processing such as machining and heat treatment which will be discussed later in the paper.

Multiple studies have shown that base plate heating can have a beneficial effect on the residual stress profile. Figure 1.17 details a study performed by Mercelis. The darker bars represent the normal stresses in the x and y (horizontal) directions and clearly show a reduction in stress magnitude as a result of an initial base plate temperature of 200 °C. While the stress reduction is rather mild, it can be expected that an increase in the base plate temperature will result in a continuation in the reduction of residual stresses.

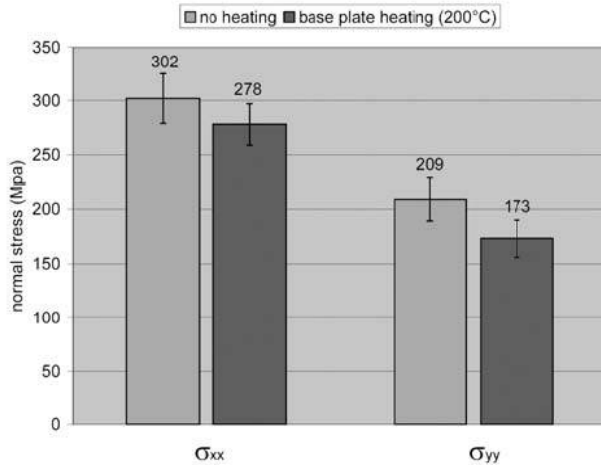


Figure 1.17 Influence of base plate heating [21]

Additionally, when considering the scanning strategy used, shown in Figure 1.18, a correlation can be clearly determined between the laser scan direction and the resulting residual stresses. According to Figures 1.17 and 1.18, it can be seen that the higher residual stresses result in the direction normal to the scan direction. In this case, the laser scanning along the y-direction results in a higher residual stress in the x-direction.

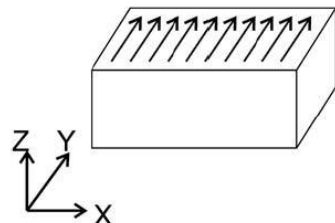


Figure 1.18 Scanning Strategy (w. data in Figure 16) [21]

Figure 1.19 reinforces the analysis of Figure 1.17. It shows part distortion in the vertical direction (displacement) on the y-axis and the position of the measurements along the part on the x-axis. The part was made through SLM and had a shape shown by the model presented in

Figure 1.20. From this, Figure 1.19 clearly shows that a reduction in initial platform temperature, to 100 degrees Celsius and then to the ambient temperature of 20 °C causes increased deformation in the z-direction. This deformation can also be seen to relate logically to an increased bend in the cantilever part.

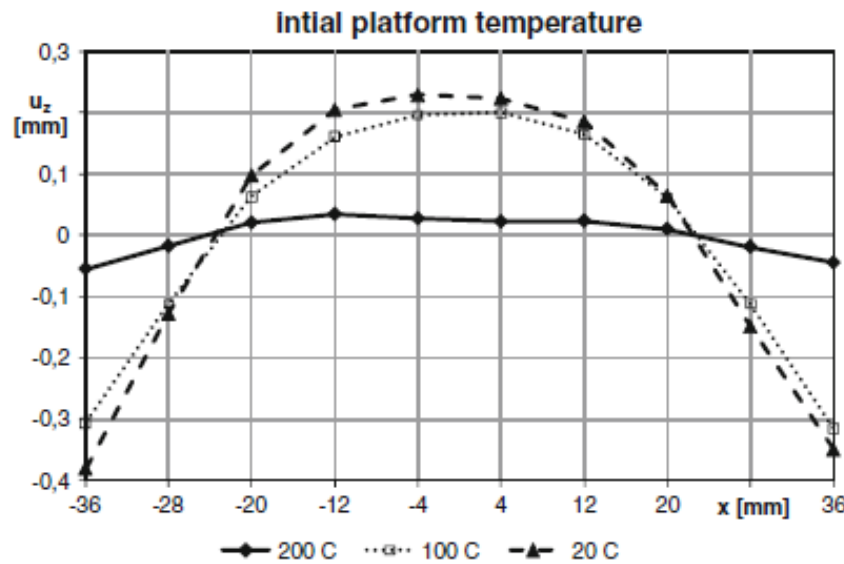


Figure 1.19 Distortion vs. Initial Platform Temperature [13]

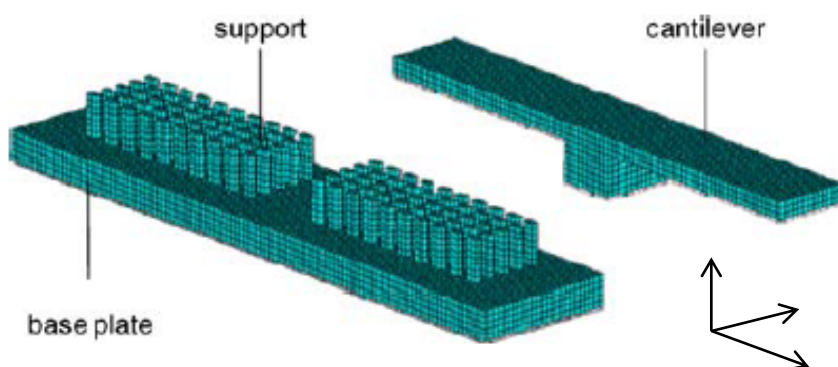


Figure 1.20 Base-plate, supports, and part geometry [13]

1.1.5.8 Influence of Scanning Strategy

One of the most critical factors found to impact the properties of the final part is the scanning strategy used by the laser. Scanning strategy refers to the approach and optimization of the laser's path to properly melt the material. Different strategies can result in different resultant residual stresses, and thus different deformations. Zaeh compared the effects of 4 different scanning strategies, shown in Figure 1.21. The first three strategies are similar, long scanning in the x-direction, y-direction, and then long scanning in both the x and y-directions, alternating by layer. The final strategy is called island scanning, and is depicted by Figure 1.21b.

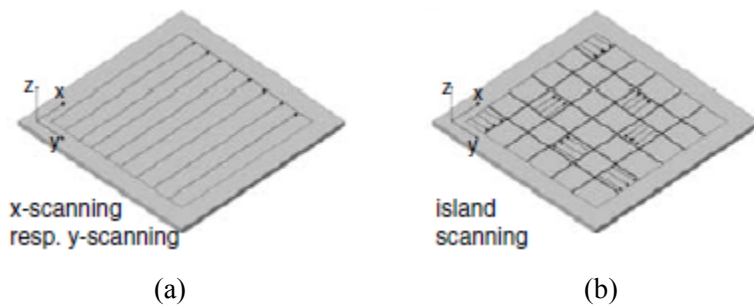


Figure 1.21. Scanning Strategies [13]

The results of these strategies on the residual stress profile are shown in Figure 1.22. Figure 1.22a shows the effect of different scanning strategies on normal residual stresses at the upper surface along the x-axis of the part (shown in the bottom right of the figure) and Figure 1.22b shows the effect on normal residual stresses in the z-direction at the middle of the part. Looking at Figure 1.22a, the highest longitudinal stresses were attributed to scanning along the x-direction. This is logical considering the shape of the part, with a much greater length in the x-direction than in the y. Next was the x-y alternating scanning strategy.

Island scanning was found to result in the lowest residual stresses due to the distributed energy input.

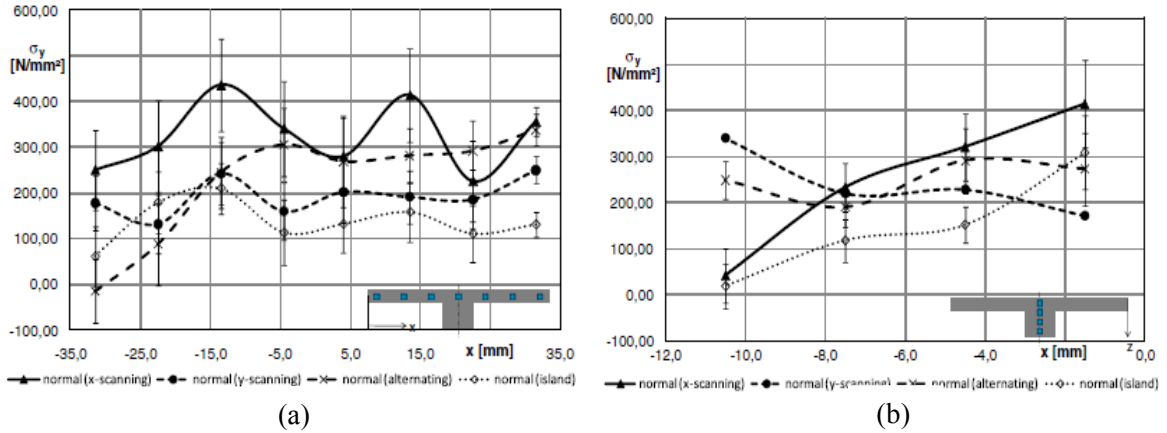


Figure 1.22. Normal Stresses on the cantilever in the (a) horizontal dir.; (b) vertical dir. [13]

Figure 1.22b relates similarly to Figure 1.22a with the lowest resultant stresses occurring under island scanning. Scanning in the y-direction and alternating scanning are found to have lower residual stresses on the part surface, however as the profile is measured with decreasing z, the island scanning strategy is found to be superior. The difference in expectation at the surface may result from the short y-axis relative to the x-axis.

In order to better compare the effects of scanning strategy, it may be better to look at a square part so that the effects of scanning in the x and y directions are normal to each other but similar in their effects. Kruth detailed such a comparison in 2004 [12]. Figure 1.23 shows the six different scanning strategies used. Strategies 1 and 2 are just normal scanning in the x and y directions respectively. Scanning strategies 3 and 5 start with scanning in the x-direction in the bottom left quadrant, and switch to y-scanning and then back in each successive quadrant. Strategy 3 uses a 5 mm × 5 mm quadrant division and Strategy 5 uses a 2.5 mm × 2.5 mm quadrant division. Strategies 4 and 6 use a method called LHI or least heat influence. For this

method, a selected sector is randomly chosen as the starting sector. The next sector is chosen based on which sector was least heated by the previous scan. Additionally, the orientation of the line is alternated from x to y between each subsequent sector. Again, Strategy 4 uses a $5 \text{ mm} \times 5 \text{ mm}$ quadrant division and Strategy 6 uses a $2.5 \text{ mm} \times 2.5 \text{ mm}$ quadrant division. Kruth compared these 6 strategies in two ways: scanning directly on the base plate and melting one powder layer (with thickness of $150 \mu\text{m}$) on top of the base plate.

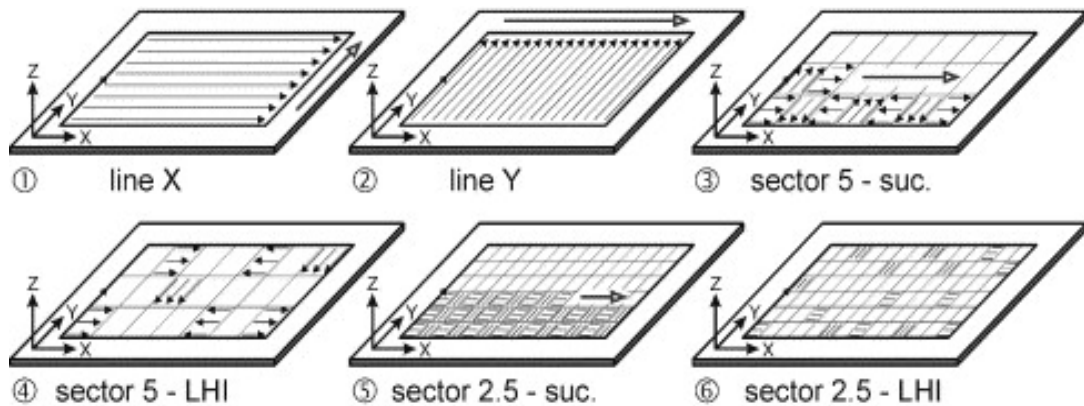


Figure 1.23 Scanning Strategies used for Comparison [12]

Figures 1.24a and 1.24b show the results of these tests. In both Figures, the black bars represent the effect on just the baseplate and the white bars represent the effect on the baseplate with the $150 \mu\text{m}$ powder layer. The immediate finding in the comparison between the two figures is that scanning along the x-direction results in the smallest curvature in that direction but the highest curvature in the y-direction while scanning along the y-direction results in the highest curvature in the x-direction but smallest in the y-direction. Additionally, sector wise scanning (scanning strategies 3-6) result in less deformation, with no major differences between the large (3 and 4) and the small (5 and 6) strategies. Kruth notes that despite the lack of difference,

smaller sectors need less energy input from the laser in order to reach the same melting behavior and temperature as the larger sectors. This reduced energy input would similarly reduce any deformations caused by the thermal gradient and associated mechanisms, favoring smaller sectors. When comparing the successive strategies versus the LHI strategies, successive was found to be preferable. Kruth speculates that this is due to a higher gradient in LHI scans. Since each successive scan is chosen based on having the lowest temperature, a higher temperature gradient will be needed in order to cause complete melting of the sector. This may enhance deformations due to the thermal gradient. Conversely, in successive scanning the previous scan serves to effectively preheat the next scanning sector, reducing the thermal gradient and associated deformations as a result.

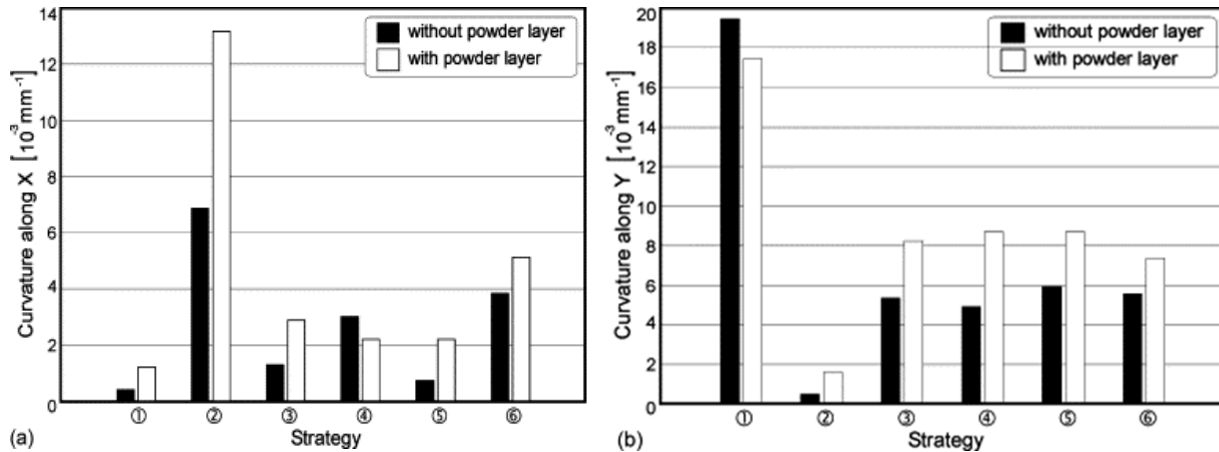


Figure 1.24. Curvature along X-axis and Y-axis vs. Strategy [12]

1.1.5.9 Fatigue Performance

A major limitation of additively manufactured metal parts is the poor fatigue life in comparison to traditionally manufactured parts. This is one of the main reasons why additive manufacturing of metal parts is effectively stuck in the rapid prototyping phase, with limited use

in commercial products with some exceptions. The fatigue life of the part is affected by a number of factors and mechanisms such as tensile residual stresses, build direction, and the microstructure of the part. The most important defect affecting the fatigue life, however, is porosity as this is the most likely site for crack initiation. Since the majority of fatigue life deals with the incubation of a crack (followed by the crack's propagation), reducing the effects of the mechanisms for crack initiation improves the fatigue performance. This can be done through post processing techniques like peak-hardening which serves to homogenize the microstructure and eliminate any heat-affected zones. Figure 1.25 shows graphically how tensile residual stresses assist crack initiation by applying a preliminary stress in the part.

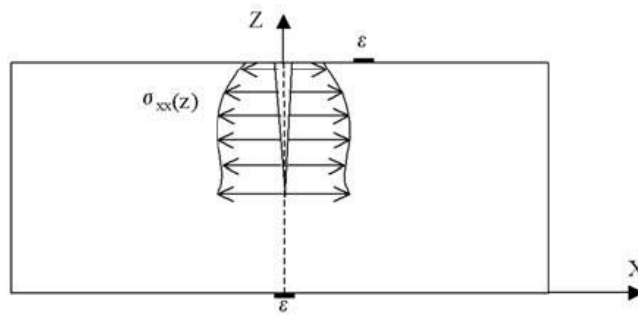


Figure 1.25 Tensile Residual Stress Crack Initiation [21]

Brandl performed fatigue tests comparing S-N curves for each of the samples shown in Figure 1.26. The variables being compared were samples made with an initial platform temperature of 30 °C and 300 °C, building direction in the 0°, 45°, and 90° directions, and peak hardening (T6). The samples were made using the SLM method with ALSi10Mg powder with particle size in the range of 25-45 microns. The use of platform preheating to 300°C was expected to reduce residual stresses by lessening the thermal gradient present during the SLM process. The T6 peak hardening process was characterized by:

- Solution heat treatment for 6 hours at 525 °C.
- Room temperature water quench.
- Artificial aging for 7 hours at 165°C.

This process was chosen in order to create samples with maximum tensile and yield strengths and adequate elongation. The samples were peak-hardened before final machining in order to remove defects in the surface layer.

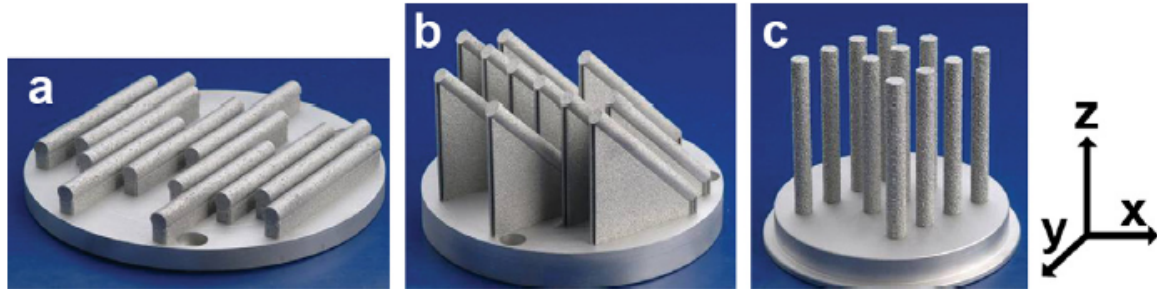


Figure 1.26 Samples (static tensile) built in different directions: (a) 0°, (b) 45°, and (c) 90° [23]

Table 1.4 shows the amount of samples in each batch and how each batch was made. As mentioned before, the variables to be observed and contrasted are platform temperature, building direction, and whether or not the sample was peak-hardened.

Table 1.4 Details of the Sample Batches [23]

Batch number	# of Samples	Platform Temp. (°C)	Building Dir. (°)	Peak-Hardened (T6)
#10	12	30	0	Yes
#11	10	30	90	Yes
#12	10	30	45	Yes
#13	9	300	0	No (as-built)
#14	10	300	0	Yes
#15	10	300	90	No (as-built)
#16	10	300	90	Yes
#17	10	300	45	No (as-built)
#18	10	300	45	Yes

Figures 1.27 and 1.28 show the results of this testing by comparing the maximum stress to the number of cycles until failure. The testing was conducted with a stress ratio of 0.1, meaning this is a tensile-tensile test and that the minimum stress was 10% of the maximum. Figure 1.27 compares the effects of building direction on the fatigue life. The platform temperature is kept constant at 30°C and all samples tested were peak-hardened. From this figure, it can be seen that the 0° building direction had a significantly higher fatigue resistance than the 45° and 90° building directions (which were comparable to each other). Looking at Figure 1.26, this can be attributed to the layer orientation's relation to the load direction. Since this is a tensile test, the initial build direction is orthogonal to the load direction, meaning imperfections and tensile residual stresses play less of a role in fatigue resistance.

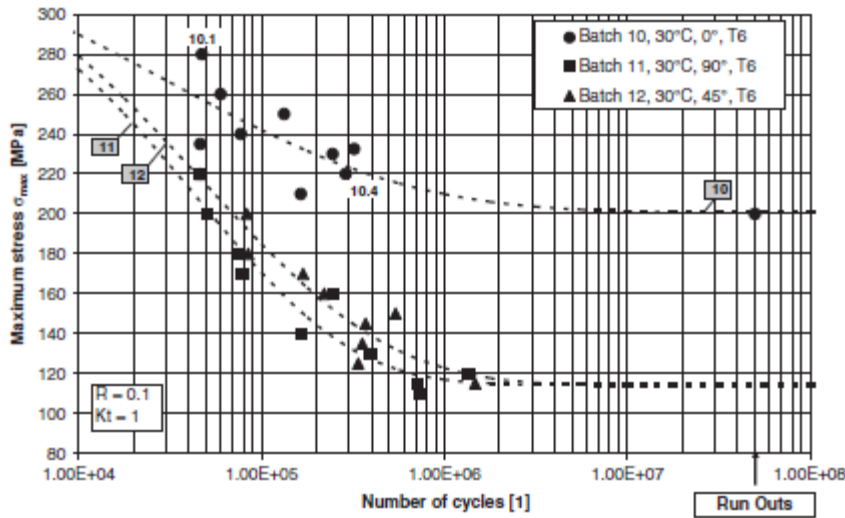


Figure 1.27 Fatigue Resistance of batches built at 30°C platform temperature [23]

Figure 1.28a is used to compare the effects of building direction and peak hardening on the fatigue life. All of the samples tested were made with an initial platform temperature of 300°C, so this is not a factor being tested in this figure. Comparing the data in Figure 1.28a, it can be first readily observed that T6 peak hardening has a distinct positive effect on the S-N curves for all building directions and that building directions play a much smaller role in fatigue life when the parts are made with an initial platform temperature of 300°C. In comparison to the analysis of Figure 1.25, this is because a higher initial platform temperature helps to avoid imperfections and residual stresses in the final part. Comparing the two figures, it can be seen that the 0° building direction has a very mild increase when the platform temperature is increased. This is because the imperfections and stresses are parallel to the loading direction, giving them the smallest possible notch-effect. Conversely, the 45° and 90° building direction's fatigue resistance increases greatly with increased platform temperature, as imperfections play a much larger role in crack initiation and propagation. Figure 1.28b compares samples that have all been peak hardened but are of varying build direction and platform temperature. This figure

reiterates and reinforces what was said before: the fatigue resistance of the 45° and 90° samples is considerably increased when built with a higher platform temperature.

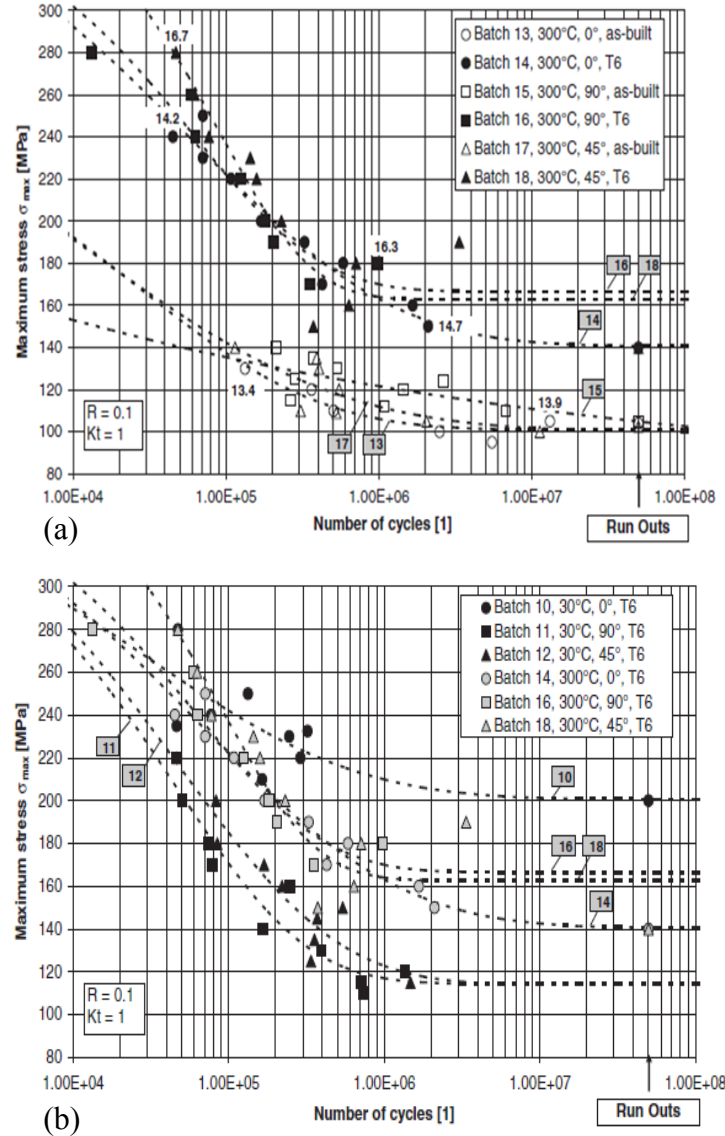


Figure 1.28 Fatigue Resistance of batches (a) 300°C platform temp.; (b) peak hardened [23]

1.1.5.10 Wear Performance

In addition to fatigue, although not to the same extremity, the wear performance of AM-manufactured parts also serves as an area of possible improvement. Kumar and Kruth investigated the fretting wear of a number of SLM developed parts in order to determine and compare their performance [24]. Table 1.5 shows the different materials used for the tests.

Table 1.5 Materials and Machines used for Fretting Tests [24]

#	Materials Name	Trade Name	Source	SLM Machine
1	Concept Stainless Steel	CL20ES	CL GmbH	KUL
2	Concept Tool Steel	CL50WS	CL GmbH	CL
3	EOS Stainless Steel	17-4	EOS GmbH	CL
4	Ti-6Al-4V	CL 40Ti	CL GmbH	CL
5	Co-Cr-Mo	-	MTM	CL

In addition to those listed above, Kumar and Kruth also tested materials made through the SLS process. Those materials are LaserForm ST-100, a polymer coated steel powder, and DirectSteel 20 V1. Fretting is a specific type of wear which occurs that occurs due to rubbing on a contact surface. In this case, the parts were linearly oscillated while a counter body was kept fixed, causing the part to gradually degrade. For the purpose of this test, the load cases were 2, 4, and 6 N, with a linear sliding distance of 200 microns and a frequency of 10 Hz. Each part was subjected to 1×10^4 cycles.

The results of these tests are not quantitatively displayed due to the amount of data, however the implications of these results are discussed. The coefficient of friction for all samples was found to vary between 0.5 and 0.8, decreasing with increasing load. In addition to the materials discussed above, multiple conventionally manufactured tool steels were also tested for comparison. Among the stainless and tool steels made through SLM, the Concept Stainless steel

was found to have the highest wear resistance (with a wear volume of $51 \times 10^3 \mu\text{m}^3$ from the 6 N load case), closely followed by the EOS stainless steel (with a wear volume of $66 \times 10^3 \mu\text{m}^3$ from the 6 N load case). The concept tool steel had the lowest wear resistance (with a significantly greater wear volume of $462 \times 10^3 \mu\text{m}^3$ from the 6 N load case). This shows that the wear resistance of SLM parts made from steel actually decreases with an increase in hardness. The performance of the LaserForm ST-100, made through SLS, was found to be much better than those of the SLM steels previously mentioned (with a wear volume of $29.6 \times 10^3 \mu\text{m}^3$ from the 4 N load case). Next, the materials made for use in the bio-medical industry fared much worse in the wear tests, however this is not their purpose. These materials include Ti-6Al-4V (which had a wear volume of $9337 \times 10^3 \mu\text{m}^3$ from the 6 N load case) and Co-Cr-Mo (which had an improved wear volume of $2252 \times 10^3 \mu\text{m}^3$ from the 6 N load case).

Some comparisons to note are that the iron-based AM parts performed better than the conventionally produced milled tool steel, giving rise to the ability of AM techniques to produce parts with properties and performance superior to conventional methods. The coefficients of friction for all the materials were also notably high, meaning that there exists room for improvement on this facet. Additionally, Kumar and Kruth noted that the parts were not at full density, implying that better performance could be achieved with improved part density. Also, the high wear resistance of the LaserForm ST-100 shows that the SLM process may not always be superior to the SLS process, and demonstrate that these processes' differences and effects should be further investigated.

1.2 Review of Machining of LAM Metal Parts

1.2.1 Machining Processes

When considering the problem of dimensional accuracy for AM parts, machining is an obvious choice for insuring crisp and accurate dimensions, and avoiding common defects like the staircase effect. In addition, different machining processes can also serve to mitigate surface integrity defects like roughness, residual stresses, and micro-cracks. The combination of additive and subtractive manufacturing processes can be referred to as a hybrid manufacturing process chain, combining the sustainability and design freedom of additive manufacturing with the dimension and surface finish of subtractive manufacturing. The three subtractive methods most regularly used for this are turning, milling, and grinding.

1.2.2 Surface Integrity

Surface integrity of a part depends on many factors, however the two most significant are residual stresses and microhardness [25]. In addition to the most obvious benefit of machining post-processing for dimensional accuracy, other factors such as surface finish, residual stresses, micro-cracks, and hardness can benefit from machining as well.

Brinksmeier performed experiments on SLM parts to assess surface integrity after grinding with two different sets of parameters and milling. The two sets of grinding parameters consisted of one aimed at utilizing the grind-strengthening effect and one aimed at reducing thermal impact (CBN grinding). The milling process was performed with a 65 mm inserted blade cutter. The SLM parts, made out of 18 Maraging 300, were built with both horizontal and vertical orientations and were compared against the conventionally manufactured AISI 52100 [26].

1.2.2.1 Roughness

Figure 1.29 shows Brinksmeier's results on roughness Ra values of the different materials. For all materials tested, CBN grinding resulted in the highest Ra values while the grinding parameter A (focused on the grind strengthening effect) resulted in similar Ra values as milling.

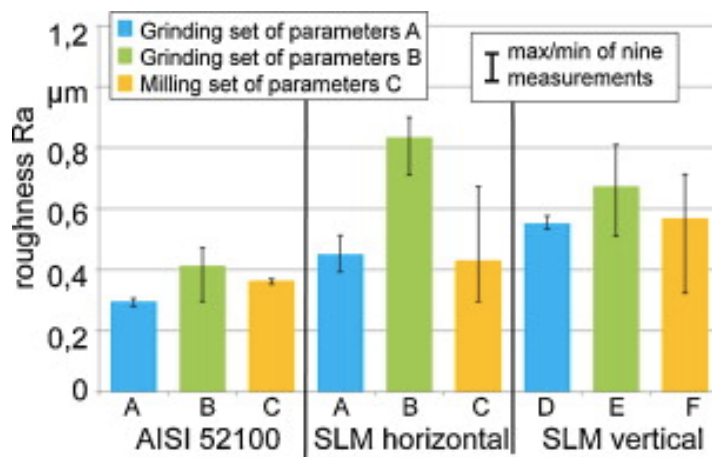


Figure 1.29 Surface roughness of samples [26]

1.2.2.2 Hardness

Brinksmeier tested the Vickers hardness of each of the different samples and parameters using ISO 6507-1 with a load force of 0.098 N. However, the hardness values were found to be highly similar for all machining parameters. Figure 1.30 shows the HV measurements for the CBN-grinded samples. The overall finding of this figure is the limit of depth influence of grinding to be 40 microns. Brinksmeier attempted to have a more accurate shallow-depth measurement by decreasing the load case by half to 0.049 N; however no changes in hardness values were discovered.

Brinksmeier also notes the correlation between porosity and hardness values, and as such the selection of process parameters are integral to the final properties of the part.

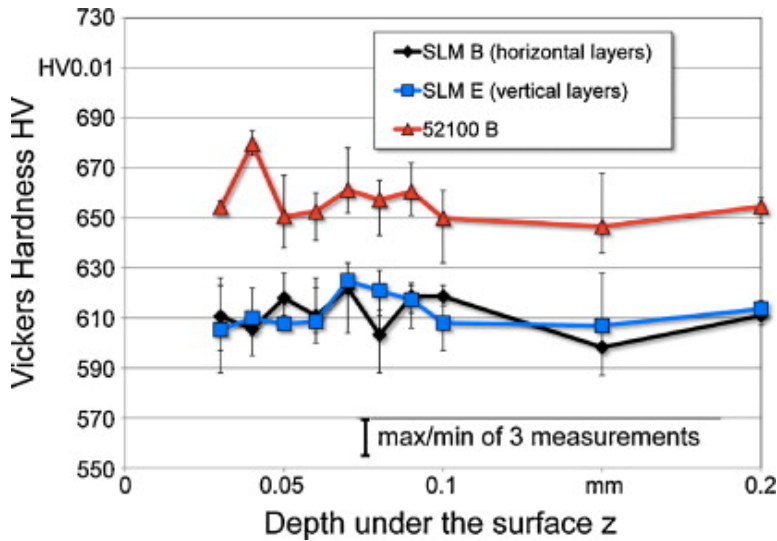


Figure 1.30 Hardness depth measurements [26]

1.2.2.3 Residual stress

Brinksmeier used XRD to measure residual stress depth profiles within the first 250 microns. Figure 1.31 shows the results of this testing. Each parameter was tested on three identical samples and the mean values are shown in the figure.

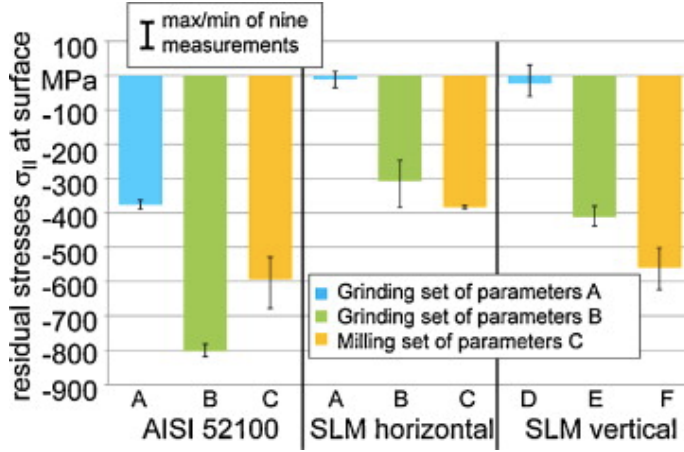


Figure 1.31 Residual stresses on surface [26]

This testing found the CBN grinding to lead to the highest compressive stress values in the AISI 52100, while the milling process lead to higher compressive stresses in the SLM produced parts. In all cases, the grind-strengthening parameter resulted in the lowest compressive values.

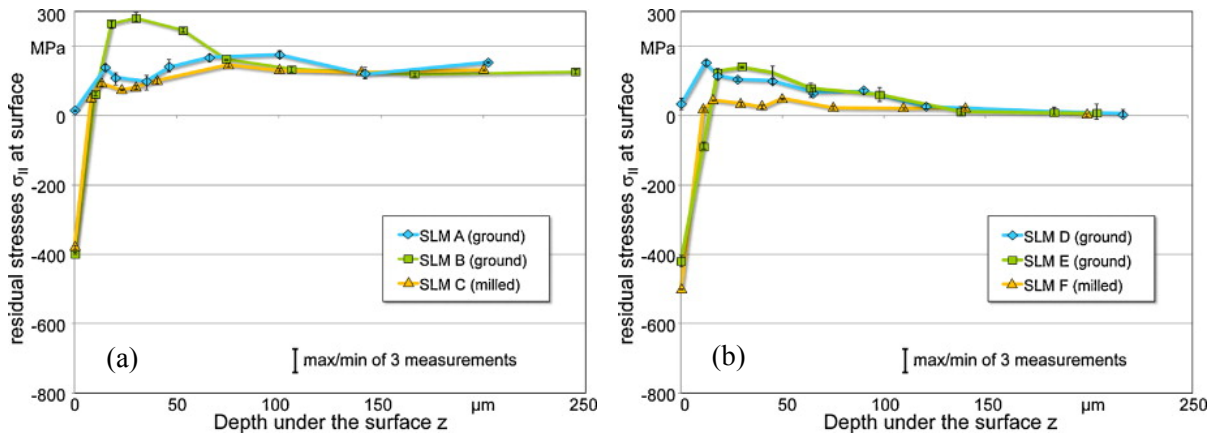


Figure 1.32 Residual stress profiles of SLM-samples with (a) horizontal and (b) vertical layer orientation [26]

Figures 1.32 shows the residual stresses of the horizontally and vertically oriented SLM parts respectively. These figures show that samples with horizontal layer orientation had tensile residual stresses at depth after machining while samples with a vertical layer orientation had stresses close to 0 MPa at a depth of 100 or more microns. It can also be seen that both CBN grinding and milling of the surface resulted in compressive residual stresses of 400-500 MPa, while the grind-strengthening grinding resulted in stresses around 0 MPa or slightly higher (more tensile). Figure 1.33 shows the same plot but for the conventionally manufactured AISI 52100.

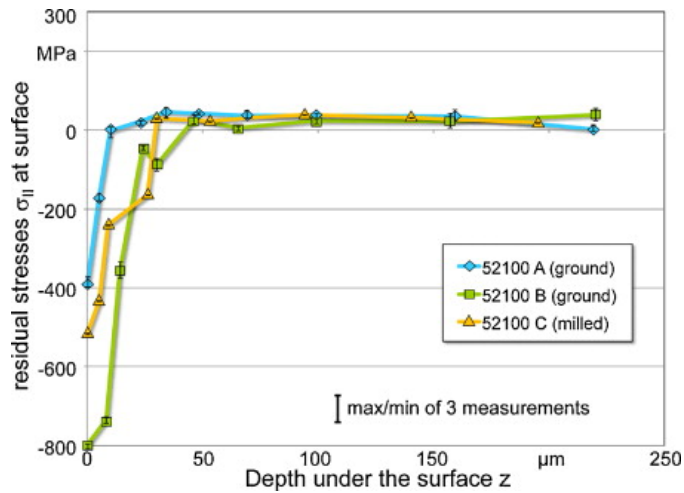


Figure 1.33 Residual Stress Profiles of AISI 52100 [26]

This figure shows that the conventionally manufactured processes results in less tensile residual stresses in the part. It also succeeds in showing the depth abilities of each of the different types of grinding and milling processes. From this, it can be seen that the CBN-grinding has the largest depth effect, followed by milling. This means that grinding can be an effective tool for imparting compressive residual stresses to counteract the tensile residual stresses inherent in AM techniques.

1.3 Summary of Review

AM has continued to dramatically improve since its development in the late twenty-first century. As process parameters and post-processing techniques continue to develop and improve, the usefulness and breadth of influence of these techniques will continue to expand as a result. This has been shown and proven by the volume of research into biomaterials such as Ti-6Al-4V as well as by the current use of products by GE in commercial industries. AM represents an increase in the design freedom of engineers and can result in many improvements and breakthrough in a number of industries as its processes continue to improve. While some notable defects and issues still plague AM metallic materials, the continued research and study into this set of new processes will serve to only increase and improve the mechanical properties and critical issues relative to conventionally manufactured parts.

There are many different areas for improvement in AM processes. Some of the most critical for AM to have a large industry effect are quality assurance (through process monitoring), increase in the number of possible materials, process optimization for any new materials (in order to have near full part density and avoid defects like the balling effect), and further research into the effects of different post-processing techniques on the overall part performance. While heat treatment techniques are known to provide a substantial increase in fatigue performance due to the relaxation of the residual stresses and reorientation of the microstructure, little is quantitatively known about the influence of machining processes on a parts fatigue life. Brinksmeier showed that methods such as CBN-grinding and milling resulted in compressive residual stresses at the surface and improved Ra values. It can be logically assumed that these processes would also have a beneficial effect on the fatigue life as well; however this is a statement that needs to be tested and quantified.

CHAPTER 2

EFFECTS OF MACHINING ON THE SURFACE INTEGRITY OF IN718 MADE BY SELECTIVE LASER MELTING

2.1 Introduction

The additive manufacturing of metallic parts is a relatively new technique that allows increased design freedom. The most widely used AM process to manufacture metal parts is selective laser melting (SLM), a process consisting of the use of a laser to melt metallic powders in a layer-by-layer fashion. Figure 2.1 provides the schematic of a typical SLM machine.

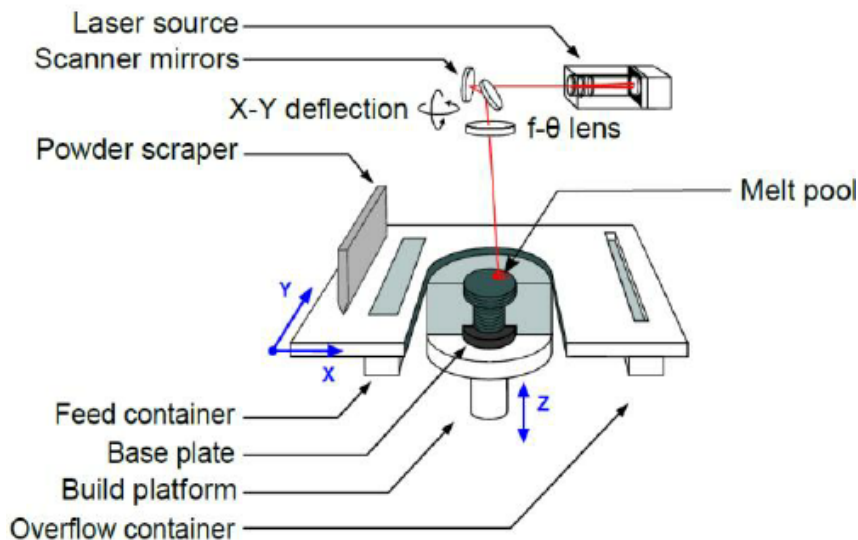


Figure 2.1 SLM schematic [27]

While SLM allows new freedoms and possibilities in terms of design, there exists a number of limitations due to the nature of the process. Most of these limitations arise from the high thermal gradient of the melt pool, which leads to poor dimensional accuracy, high surface roughness, high porosity, and tensile residual stresses.

In order to further realize the potential of SLM as a design tool, strides need to be made in order to minimize the effects and occurrence of the limitations mentioned above. This improvement can be manifested in two ways: optimization of the process itself and improvement of a SLMed part through post-processing. Many studies have focused on optimizing process parameters such as laser power, laser speed, powder depth, substrate temperature, and scanning strategy as discussed in Chapter 1. Additionally, the effects of post processing techniques such as heat treatment have been studied for a number of metallic powders and processes as well. The use of machining as post processing, however, has yet to be studied in depth.

While the usefulness of machining process for the improvement of a SLMed part is widely taken for granted, the actual mechanisms and confirmation of this potential improvement have not yet been studied. The experimental data is expected to allow engineers to create better products, and additionally allows the validation of a process predictive model through techniques such as FEA.

The integration of machining with SLM creates a hybrid manufacturing technique that easily overcomes the problems of poor surface roughness and low dimensional accuracy inherent in a SLMed part. In this paper, the effects of machining as post-processing for SLMed IN718 samples will be studied with a focus on surface integrity. The goal is to provide the preliminary results in realizing the potential improvements of surface integrity for a SLMed part via the addition of a machining process.

2.2 Experiment

2.2.1 SLM Experimental Setup

The experimental strategy is split up into a number of steps from part creation to post processing to testing. The first of these is the manufacturing process itself. Figure 2.2 provides a picture of the set up.

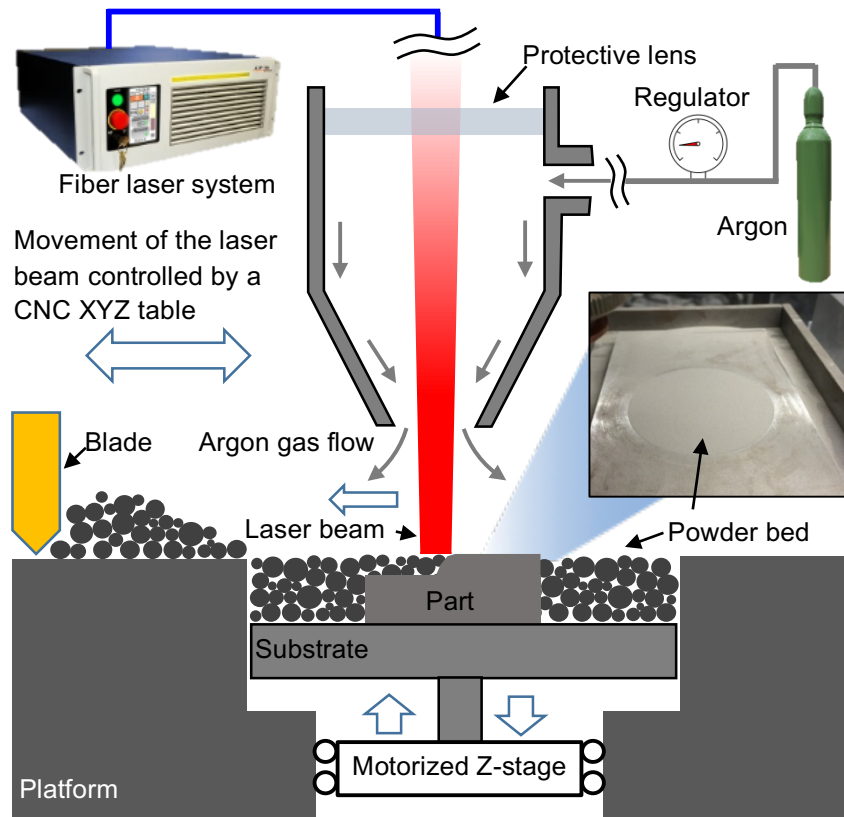


Figure 2.2 SLM set-up [28]

For this study, a Nd:YAG laser was used with a CNC unit. The Mach3 CNC program was used to relate commands to the SLM machine through the use of G-code. Argon Gas was

used as an anti-oxidizing agent in order to help improve the material properties of the part and protect the laser lens. The samples were made using gas atomization processed IN718 powders supplied by Additive Metal Alloys, LTD. Particle size analysis was performed by the supplier, and the particles were found to range in size from 16 µm to 45 µm, with 99.5% (weight by volume) of the particles being smaller than 45 µm, and 0.83% of the particles being smaller than 16 µm. Figure 2.3 shows the particle size distribution, and a columnar-like microstructure can be seen on the powder surface in Figure 2.3b.

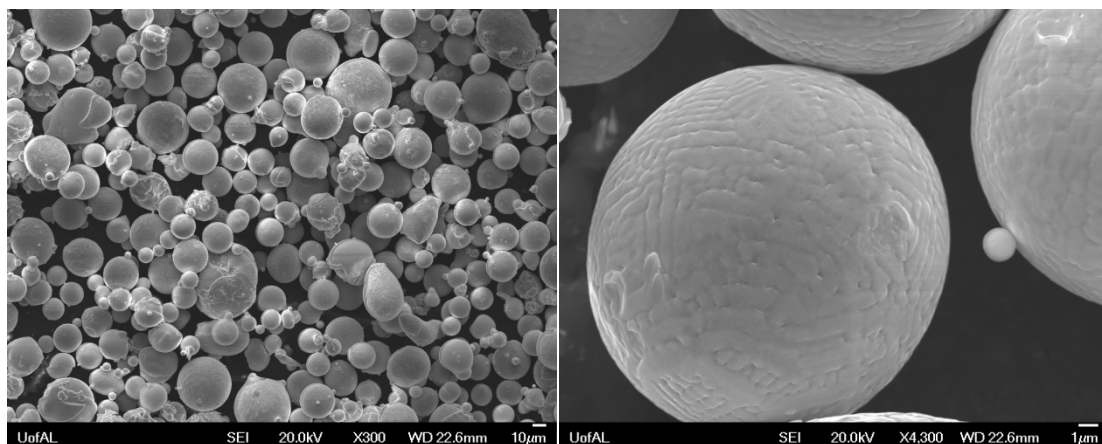


Figure 2.3 SEM images of Inconel 718 powder particles

The laser power was set at 80 W and the laser scan speed was set at 1500 mm/min, respectively. It should be noted that, due to the control of the laser's movement, the scan speed had to be accelerated after each turn, causing the laser to hover longer over sections closer to the edges. This could impact the microstructure significantly however, the experimental specimens were sectioned from the middle section with stable melting conditions.

This study explores the effects of machining (dry cutting vs. flood cutting) and its interaction with the scanning strategy used. Table 2.1 lists the scan direction and cutting type for each sample.

Table 2.1 Sample Preparation

Sample #	Scan	Cutting
	Direction	Type
1	Along Length	Flood
2	Along Length	Dry
3	Across	Flood
4	Across	Dry
5	Along Length	As-is
6	Across	As-is

Figure 2.4 shows the scanning pattern visually, where the top sample shows the scan direction along the length of the part and the bottom sample shows the scan direction across the part. Each sample was made to have the dimensions of 25 mm (L) × 10 mm (W) × 3 mm (H).

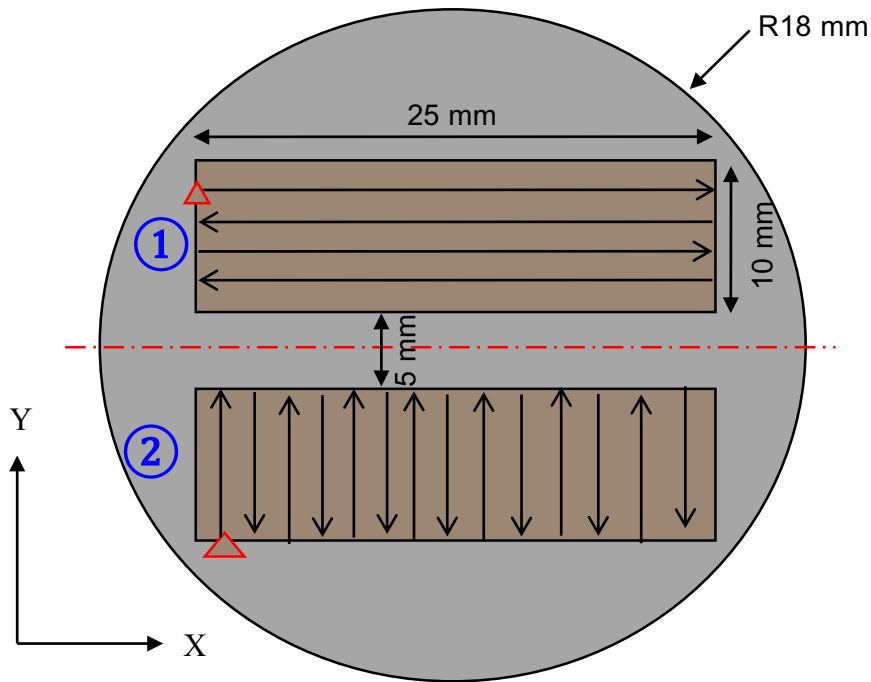


Figure 2.4 Depiction of scanning patterns

2.2.2 Milling Experimental Setup

The first step of the machining was to smooth the part. Next, each sample was machined according to the specifications in Table 2.1, with one sample of each scanning direction machined with coolant and without coolant. A CNC machine was used to perform the machining experiments according to the specifications in Table 2.2. The direction of the cut was along the length of the sample shown in Figure 2.4.

Table 2.2 Milling Parameters

Cutting speed v (m/min)	Feed per tooth f_z (mm/tooth)	Radial DoC a_e (mm)	Axial DoC a_p (mm)	Cutting mode
60	0.15	0.5	0.5	Down

2.2.3 Mounting Setup

In order to test the effects of machining on all planes, each sample was sectioned and then hot mounted using PolyFast powder in the Buehler SimpliMet 1000. The sectioning was performed in order to allow access to the XZ and YZ planes for each sample built. An example of this system is shown in Figure 2.5.

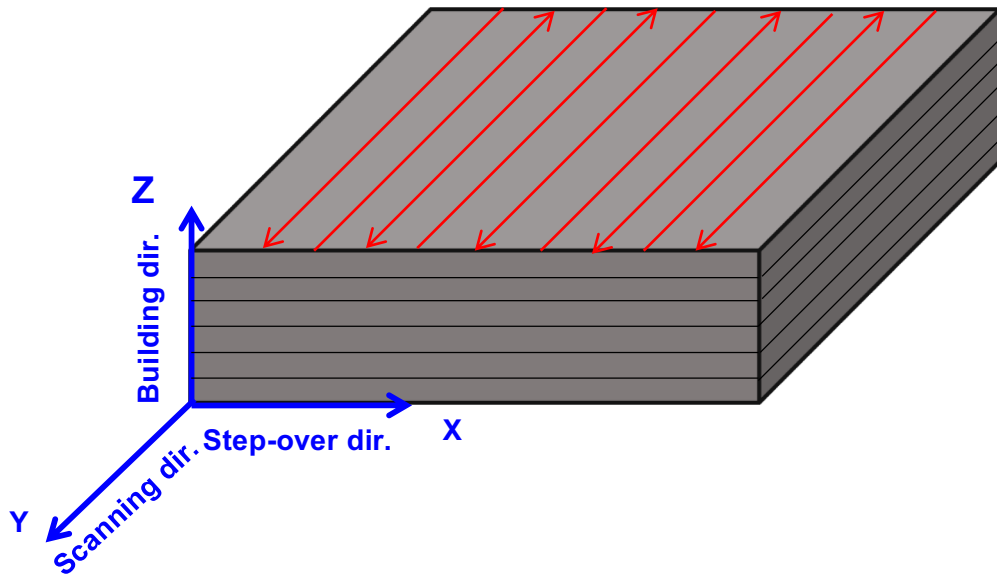


Figure 2.5 Plane Orientation for Samples

Figure 2.6 shows how the samples were sectioned, where the XZ plane comes from subsample 1 and the YZ plane comes from subsample 2.

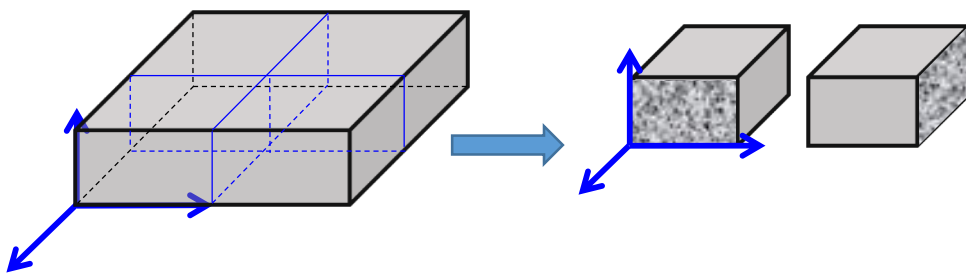


Figure 2.6 Sectioning schematic

Each sample was then polished using a 1 micron diamond suspension and then electro etched using the Buehler ElectroMet 4. These characterization steps are illustrated in Figure 2.7.

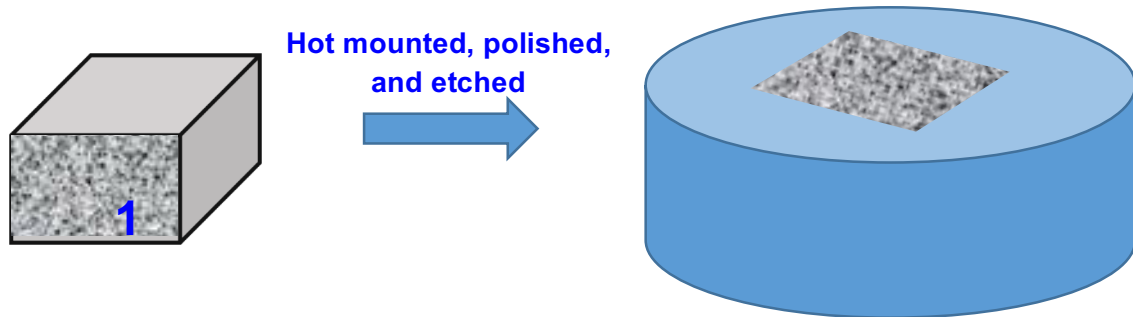


Figure 2.7 Mounting schematic

2.3 Results on Surface Integrity

2.3.1 Microstructure

The microstructure analysis yielded interesting results that weighed higher on the necessity for improving process parameters than machining. While machining a part can cause a decrease in porosity, it is the SLM itself that determines the part porosity. Additionally, it is the author's expectation that the true benefits of machining can be better realized when applied to a porosity-free part, rather than one filled with voids and other defects. A number of these defects were formed in the samples during the building phase, most notably balling and voids. Figure 2.8 shows the YZ cross-section of Sample 4, a dry machined part.

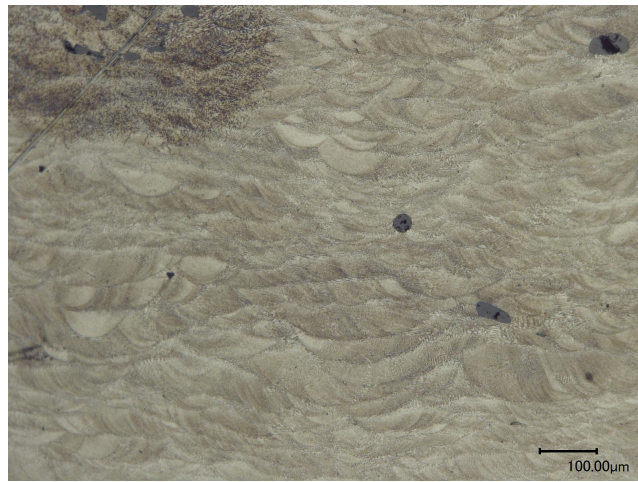


Figure 2.8 YZ-plane of Sample 4

This image shows the laser passes travelling horizontally across the page. These passes can be seen as distinctly separate from each other, with the majority of boundaries being dictated by laser passes, rather than by the naturally occurring grains in the microstructure. Some small porosities can also be seen here, with sizes ranging from 10 to 50 microns.

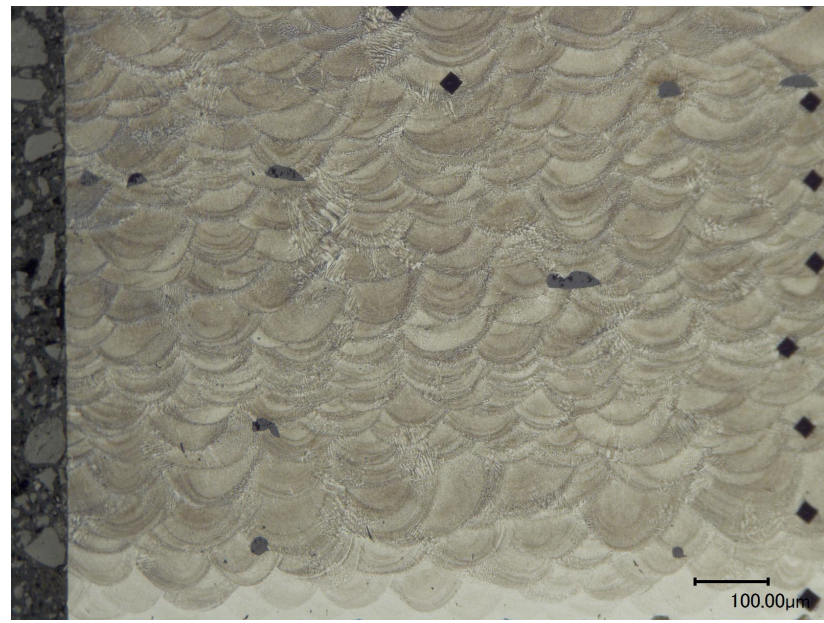


Figure 2.9 XZ-plane of Sample 5

While Figure 2.8 shows the cross-section parallel to the scan direction, Figure 2.9 shows the cross-section (XZ-plane) normal to the scan direction of Sample 5. This can be seen by the series of overlapping semi-circular patterns which are formed due to the solidification of melt pool from each laser pass. Figure 2.9 shows a uniform distribution of laser passes, with clear overlaps and limited voids. Another aspect which could be a factor which was briefly mentioned in the introduction, is the acceleration of the laser itself with each pass. While most commercial units use a scanner mechanism to achieve a near-instantaneous acceleration to the designated scan speed, the SLM machine used for this study utilized linear actuators to control movement. As such, each pass needed to accelerate and decelerate to and from the specified scan speed of 1500 mm/min. This means that the sections closer to the edges of the part (where the laser stops and changes direction) receive more thermal energy than the section towards the middle of the part. While this effect may be negligible when comparing sections of one part to each other, it becomes more noticeable when comparing the parts made with opposing scan directions, due to the dimensions of the part. Since the width of the part is only 10 mm, in comparison to the 25 mm length, the laser never achieves the optimal scan speed and spends much more time in an acceleration or deceleration phase. While this is most likely not a factor when looking at the voids, it is still a factor in the integrity of the part nonetheless.

Another notable cause of voids in the part is the balling effect. The balling effect is the tendency of a molten liquid to become a sphere due to the surface tension of the liquid. An example of the balling effect is shown in Figure 2.10.

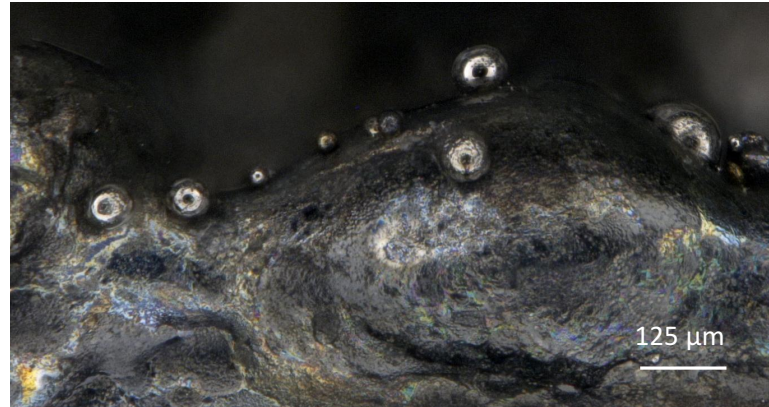


Figure 2.10. Balling Effect

As pointed out by Kruth et. al. [12], scan speed and laser power to be the two largest factors that contribute to balling. Figure 1.12a in Chapter 1 shows Kruth's theory on process parameter optimization to avoid balling.

While these investigations were performed on iron-based powders, it's likely that the same principles would apply. As such, it is highly possible that the acceleration and deceleration phases of the scan speed mentioned above could contribute to the balling effect by lowering the scan speed below the optimal window for a smooth part. Additionally, it is possible that by altering the laser power this defect could be avoided, however that hypothesis would need to be further investigated. For many reasons, the balling effect is undesirable and largely evidence of imperfections in SLM itself. Figure 2.11 shows an example of the balling effect in a void.

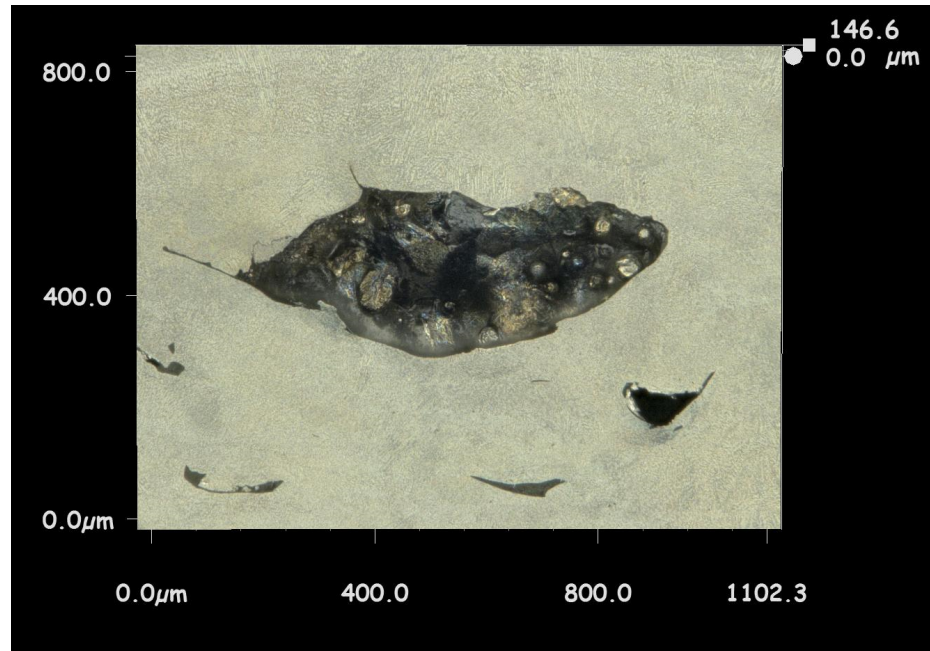


Figure 2.11. Balling Effect in XZ-plane of Sample 5

In this image, the metallic balls in the void can be seen as the culprit for its size. This void is by far the largest in any of the samples made, with a length of almost 800 μm . While multiple factors likely lead to its formation, the size in many ways was added by the formation of the balls themselves. When analyzing the depth of this void, shown in Figure 2.12 it can be seen to retreat slightly over 100 microns into the surface.

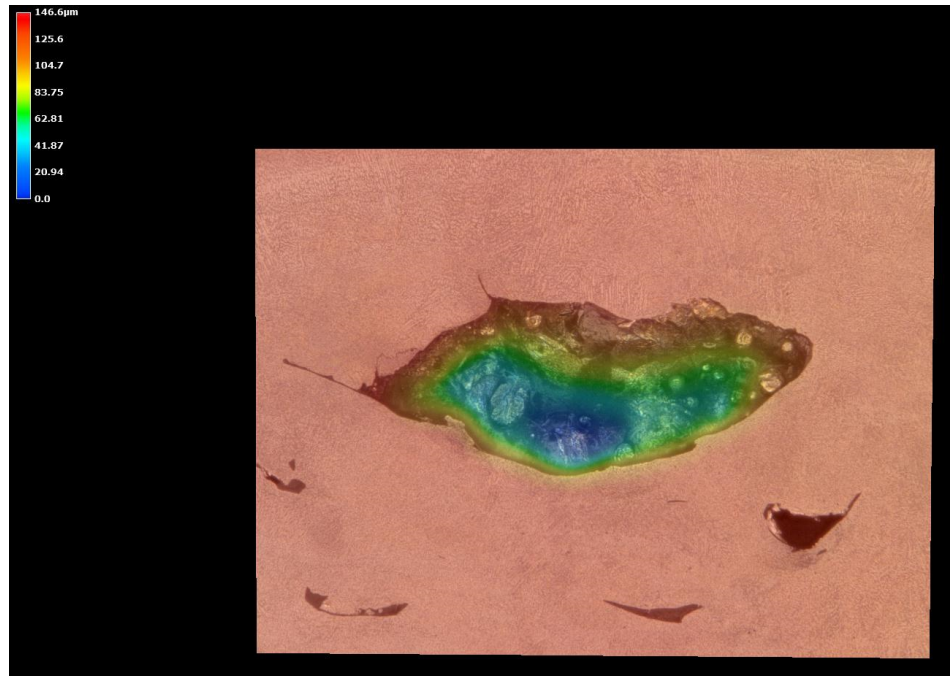


Figure 2.12. Depth Profile of Void in Sample 5

This shows one of the key reasons why further research into the SLM process is necessary as it finds its way into commercial applications. A void of this magnitude would greatly affect the fatigue life of a part, and could be a safety concern depending on the part's loading and importance.

The balling effect can also be seen in the ridges on the top surface of an as-SLMed part, as shown in Figure 2.13.

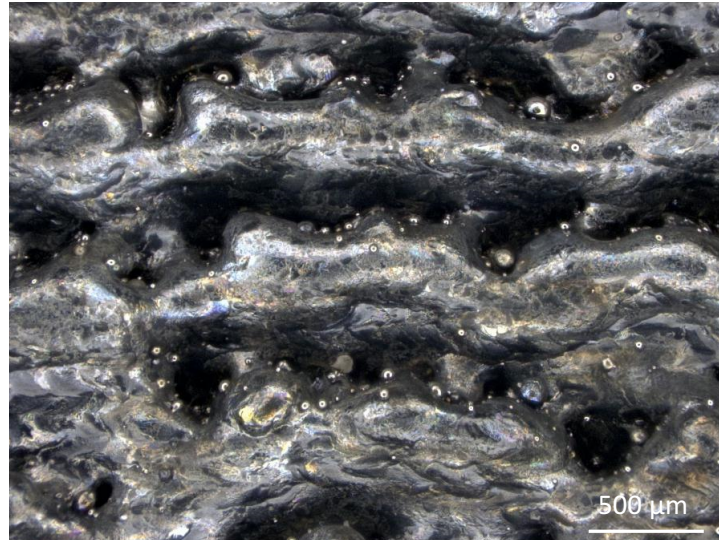


Figure 2.13. Balling Effect on XY-plane of Sample 1 Prior to Machining

2.3.2 Roughness

The roughness data was acquired using the Dektak IIA Face Profile Measuring System. Each machined sample was measured 5 times in both the X and Y directions (as per Figure 2.4), and the results were averaged. Figure 2.14 shows the colored surface topography of Figure 2.13. The change in height is not proportional to the XY directions in order to fully observe the difference.

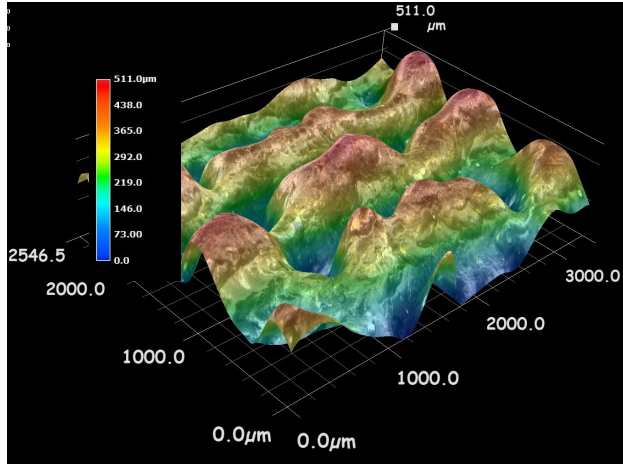


Figure 2.14. Surface Topography of Sample 1 Prior to Machining

The roughness was measured in terms of the distance between the valleys and peaks of different laser passes. If this amplitude becomes too large it is likely that only the top surface over the valleys would be fused together, creating a large void in the part. The roughness of the as-SLM samples was too large to be measured using the Dektak IIA. Looking at Figure 2.14, the roughness is found to be exceptionally high, with a total height change of 511 microns, over half a millimeter. It should also be noted that this height change is consistent across the image.

Improving surface finish of a SLMed part is where the usefulness of machining truly shines. Figure 2.15 shows the surface topography of the same sample after machining. The associated Ra values for Samples 1-4 are shown in Table 2.3.

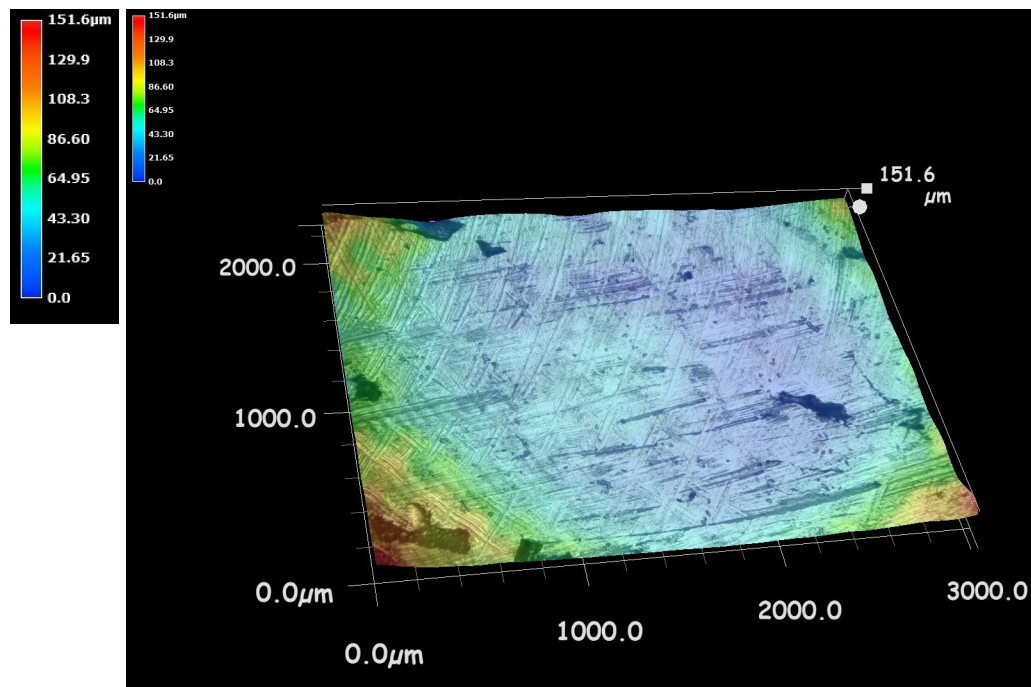


Figure 2.15. Surface Topography of Sample 1 After Machining

Table 2.3. Ra Values from Machined Samples

		Dry Machining	Flood Machining
Cutting Direction: Step-Over Direction	Measurement direction: Step-Over Direction	(0.32, 0.04)	(0.54, 0.12)
	Measurement direction: Scan Direction	(0.33, 0.08)	(0.57, 0.22)
Cutting Direction: Scan Direction	Measurement direction: Step-Over Direction	(0.39, 0.10)	(0.28, 0.10)
	Measurement direction: Scan Direction	(0.42, 0.12)	(0.52, 0.10)

The data is presented in Table 2.3 in the following format: (Average Value, Standard Deviation). From this data, three findings were made. The first is in comparing the resulting Ra

vales with Flood and Dry machining. On average, Dry machining resulted in lower Ra values by 0.113 μm , or 23.6%. This suggests that dry machining would typically create a better surface finish in SLM parts. Next the average measurements in the scan and step-over directions were compared. The Ra values were found to be lower by 0.08 μm , or 16.8%, when measured in the step-over direction. The last comparison involved investigating any possible interactions between the cutting and scan directions. This analysis found that lower Ra values occurred when the cutting direction and scan direction aligned, with a percent difference in this case of 6.8%. It should be noted that the average standard deviation was 0.11 μm , which reduces the significance of these findings. This high variability is most likely due to the irregular positioning of the porosities.

The next step was to compare the measured Ra in the SLM samples against Ra values measured in conventionally manufactured IN718. The following data was measured by Li from samples that had been machined with coolant and the same conditions as specified in Table 2.2:

- Ra measured in cutting direction: 0.15 μm [29]
- Ra measured perpendicular to cutting direction: 0.16 μm [29]

Comparing the Ra values from Traditional and SLMed samples measured in the cutting direction with coolant shows that the SLMed sample which had a cutting direction perpendicular to the scan direction has a greater Ra value by 0.39 μm and that the SLMed sample which had a cutting direction parallel to the scan direction has a greater Ra value by 0.37 μm . These values signify a percent increase of 260% and 247% in comparison to the conventionally manufactured parts. Comparing the Ra values measured perpendicular to the cutting direction shows similar results. The SLM sample which had a cutting direction perpendicular to the scan direction has a Ra value that is 0.41 μm greater than the conventional sample and the SLM sample which had a

cutting direction parallel to the scan direction has an Ra value that is 0.12 μm greater than the conventional sample. These changes represent percent increases of 256% and 75% respectively. The reason for the high Ra values in the SLMed samples is most likely due to the porosity in the parts. This porosity causes voids at the top surface, seen in Figure 2.15. On average, the SLM samples have Ra values that are 219% (or a difference of 0.33 μm on average) greater than the conventionally manufactured samples.

2.3.3 Hardness

The porosity discussed above contributes greatly to the overall variation of hardness of the samples. As part of this study, the author looked to quantify any changes in hardness values at depth due to the machining passes. Chatterjee et. al. found the hardness of an SLMed tool steel to be a direct result of the part porosity [30], and it can be assumed that the porosity of other materials plays a large role in their hardness as well. This assumption can be validated through hardness tests. Figure 2.16 shows an image of a hardness indentation test performed on Sample 3, which was machined with coolant. The parameters of all hardness tests were a load of 250 g and duration of 15 s.

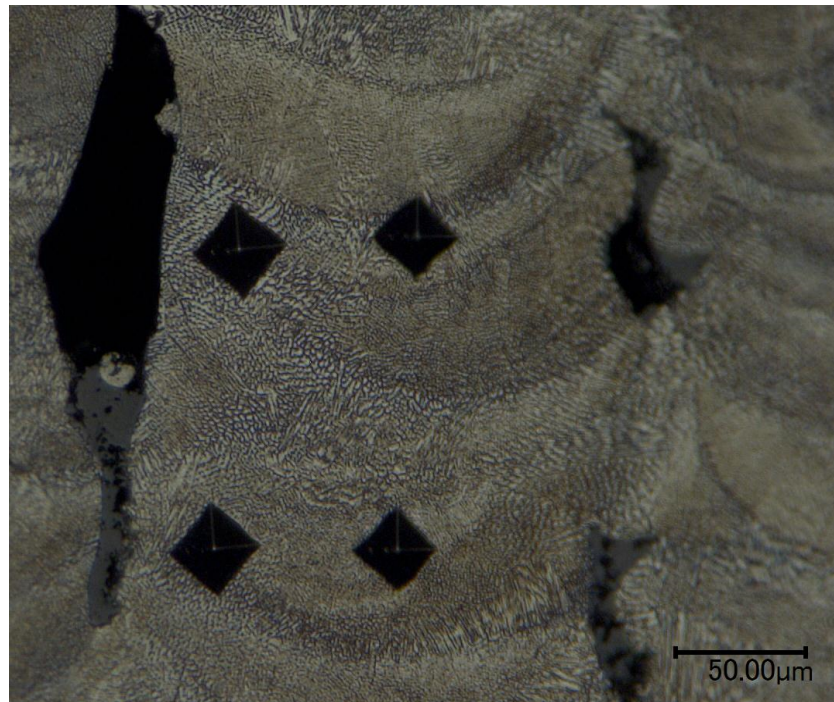


Figure 2.16 Hardness Test on YZ-plane of Sample 3

As shown in Figure 2.16, a slight increase in indentation size can be seen as a result of proximity to a void, proving the relationship between hardness and porosity. While this change in size is not entirely clear by eye, it relates to a decrease in Vickers Hardness of 108.85 HV for the top indent pair and a decrease of 118.20 HV for the bottom indent pair. This relates to a percent difference of 26.7% and 27.6% respectively. This is a high variation, especially when it is observed that each indent's location only varies by about 70 microns horizontally. There exists a number of possible reasons for this change. The first is the proximity to the porosity, as the ability of the material to support itself could be compromised by the void. The second is the edge effect, or the tendency of material to “fold over” voids during indentation tests. This next possibility is due to the γ' phase, which largely contributes to the hardness in IN718. It is

possible that imperfect melting and solidification of the IN718 particles could cause changes in the properties of the microstructure as well. Throughout the course of the hardness testing, other low hardness zones were found as well. The largest of which is shown in Figure 2.17.3



Figure 2.17 Hardness Test on YZ plane of Sample 5

In this example, the center-left indentation is notably larger than any other in its vicinity, especially those at the same depth. The difference in hardness measurement between this indent and its counterpart 84 microns to its right is about 280 HV, representing a decrease from 423 HV to 143 HV. This is decrease of 66.3%, over half of the initial hardness values. This proves the necessity for creating a repeatable initial build process when using SLM. While Hardness values can be theoretically improved at the surface through machining, the influence of porosity and voids cannot be negated.

The final area which showed fluctuations in hardness is in the area close to the substrate. In all samples tested, the lowest hardness values (excluding the outlier shown in Figure 2.17) were always found at the part-substrate interface. Figure 2.18 shows an example of this.

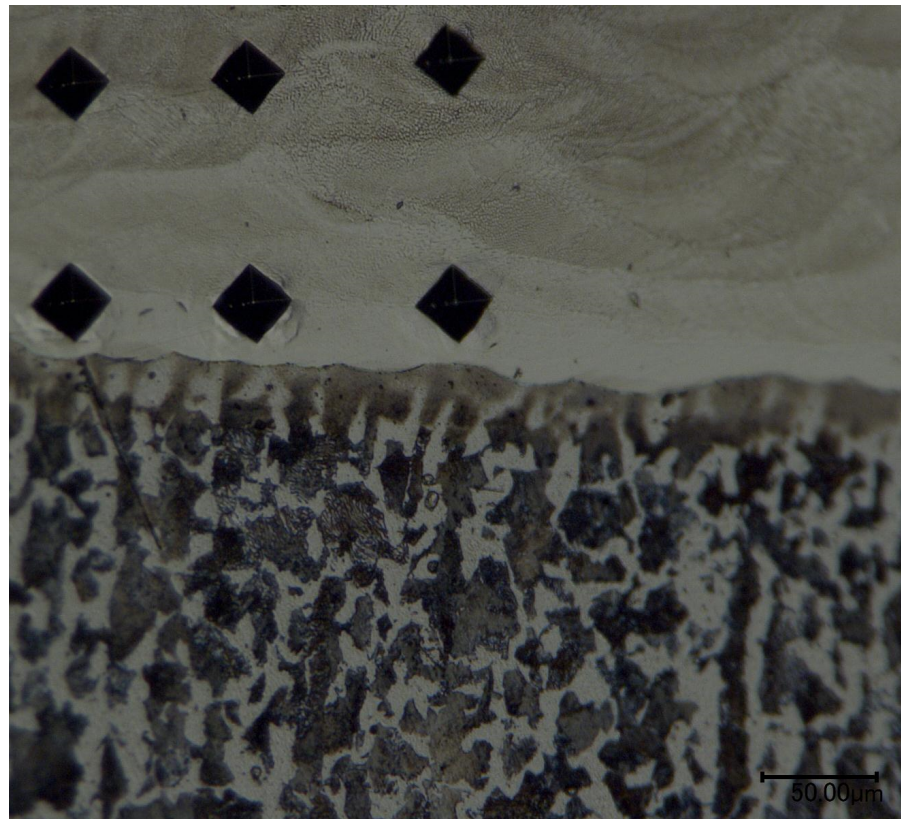


Figure 2.18 Hardness of Part-Substrate Interface on YZ-plane of Sample 5

As shown in Figure 2.19, a rippling effect can be seen around each indentation. This relates to the low hardness along the part-substrate interface. In each of the tests (excluding the outlier shown in Figure 2.17), the lowest hardness values were found on the part-substrate interface. It is likely that there are some other factors (i.e. effects of remelting) at play during the initial few layers that cause a low hardness at the interface, and the next step should be to analyze the microstructure more closely in order to see if and phases or particulates could be the

cause of the low hardness. On average, the indentations along the substrate line were 14.3% lower than those throughout the rest of the sample, representing a decrease on average from about 396 HV to 339 HV.

It was the author's objective to quantify the improvement in the hardness profile as a direct result of machining, however this was not achieved. Figure 2.19 shows the results of the full hardness profile.

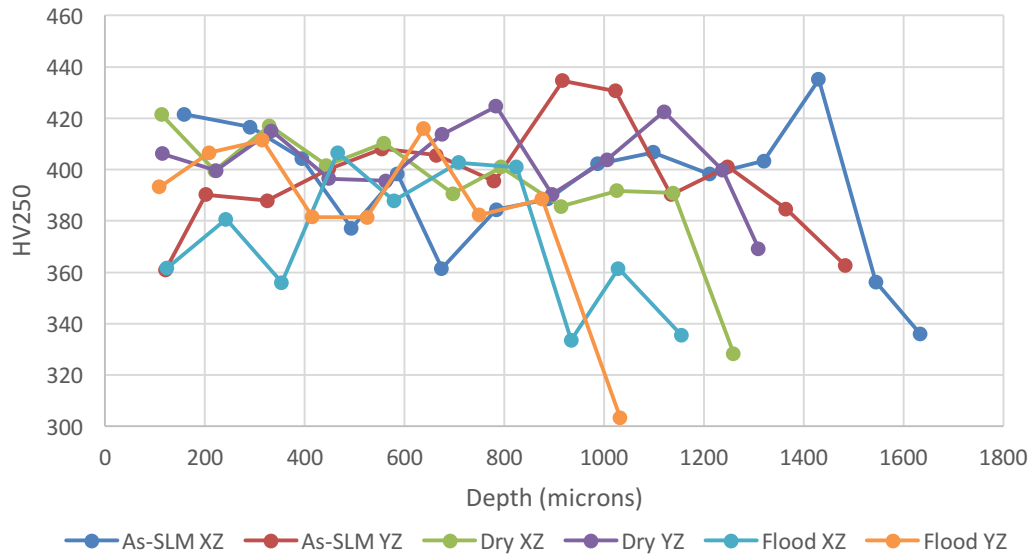


Figure 2.19 Hardness Profile of Samples 3, 4, and 5

Looking at Figure 2.19, the same general path can be seen in the hardness profile. In his test of the effect of machining on hardness, Brinksmeier found the depth of influence of machining to be around 40 microns, however he had difficulty in getting accurate measurements at this depth [26]. In this study, the same problem was encountered when using a micro-hardness indenter. Accurate readings began at around 100 μm , however there was difficulty in analyzing the hardness in the shallow depth region. Considering Brinksmeier's findings of a depth of influence of only 40 μm (when testing 18 Maraging 300, a stainless steel), it is evident that any

changes in hardness due to the machining process are hidden in this area. The fluctuations throughout the full profile of the part are most likely due to fluctuations in porosity, and it is the author's view that all of the hardness profiles shown above would approach an ideal line as the SLM process is refined and optimized. In order to accurately measure the shallow depth hardness in these samples, a nano-indenter should be used. This would allow more data collection in the shallow region, and would show and quantify any hardness changes as a result of machining.

2.4 Summary

In this study, the roughness and microstructure were successfully observed and characterized. The use of dry milling was found to result in a smoother surface on average. Other possible interactions between milling, scan, and measurement direction were identified, however the high variability of the results shows the need for repeat testing, and improvement of process parameters. The microstructure analysis showed porosities, voids, and low hardness zones in the subsurface. The high porosity experienced resulted from imperfect process parameters, and the author believes that by creating an SLM part with near-full density, a more accurate analysis of the effects of milling on a part would be possible.

The porosity and microstructure also affected the hardness profile significantly. The most significant finding was the low hardness along the part-substrate interface. The next step will be to analyze the microstructure of this interface more closely in order to identify any possible phases or particulates that may be causing the change in hardness. Also, after optimizing the process parameters to create a part of near full density and then using a nano-indenter to focus on the subsurface zone of 40 μm , the hardness profile would be much more likely to provide insight onto the exact effects of machining.

CHAPTER 3

ENERGY USAGE IN MILLING OF SELECTIVE LASER MELTED IN718

3.1 Introduction

In recent years, an increased focus has been placed on big data collection and analytics in manufacturing. This trend, known as Industry 4.0, seeks to monitor, benchmark, and optimize processes through sheer volume of data and integration of information technology into all facets of manufacturing processes.

While Industry 4.0 is mainly focused on the increased involvement of automation on the factory floor, the data collected on energy usage and analytics is of great importance as well. In addition to Industry 4.0, Sustainable manufacturing has received increased use and publicity as of late. This idea seeks to focus manufacturing optimization on minimizing energy and material usage, rather than on maximizing profits. Its basic principles and goals are best defined by the U.S. Department of Commerce as follows: “The creation of manufactured products that use processes that minimize negative environmental impacts, conserve energy and natural resources, are safe for employees, communities, and consumers and are economically sound” [31].

It is in sustainable manufacturing that additive manufacturing holds a unique opportunity. Conventional machining processes for part creation such as milling and cutting create large amounts of waste material in the form of chips and debris. The world’s entire manufacturing industry used 1,125.3 million metric tons of steel [32], 42.9 million metric tons of aluminum

[33], and 18.4 million metric tons of copper [34]. This results in a massive waste volume due to chips. Recycling these chips is financially unreasonable and ineffective [32], and these chips typically end up in a landfill.

In contrast to subtractive manufacturing such as milling, additive manufacturing builds parts layer-by-layer from powders. This allows part creation with high material utilization and additionally allots additional freedoms to design teams in terms of geometric possibilities. One of the main drawbacks of additive manufacturing is poor surface finish of the parts created, however post-processing such as milling can smooth the parts. When combined into a hybrid manufacturing route, additive-created and subtractive-milled parts greatly reduce the overall material consumption and waste of part creation.

In this study, the author seeks to analyze the machinability of IN718 manufactured through selective laser melting (SLM) by quantifying the energy consumption. This will be done by comparing the data both between milling (flood and dry milling) SLMed samples and milling conventionally manufactured IN718 samples. The goal of this chapter is to analyze the energy consumption used in order to contribute to the general knowledge and assist in the optimization of this hybrid manufacturing process.

3.2 Experiment

The samples in this experiment were made through an SLM process with IN718 powder. The process parameters consisted of a laser power of 80 W and a scan speed of 1500 mm/min. Each sample was made according to Figure 3.1.

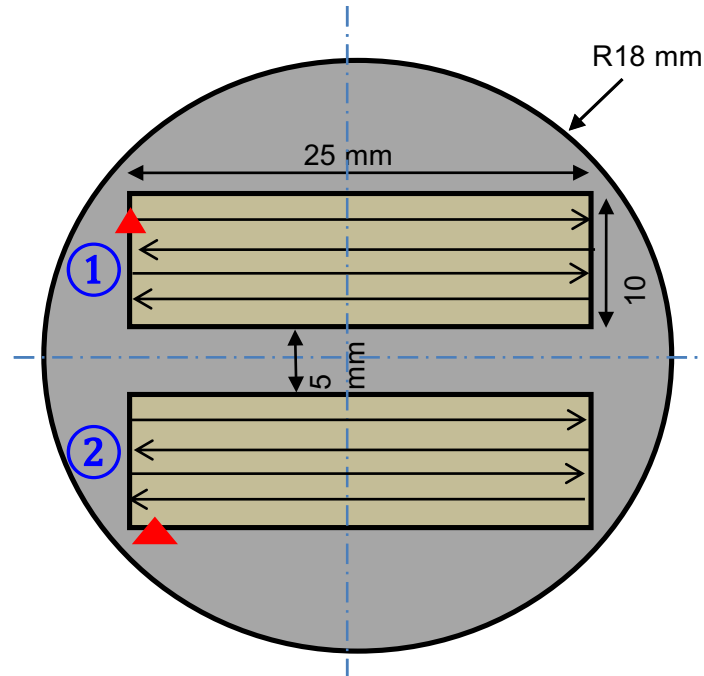


Figure 3.1 Sample dimensions

A three dimensional image of Figure 3.1 can be seen in Figure 2.5. Each sample was then milled to a flat surface according to the specifications given by Table 2.2. During the milling process, cutting power was captured and processed to obtain the energy usage using the Fluke Power Analyzer and processed in Excel.

3.3 Energy Consumption Characteristics

Two main comparisons of energy usage were made during the course of this study: dry milling vs. flood milling and milling SLMed samples vs. milling conventionally made samples. For each case, three variables were measured and used for analysis:

- Net Cutting Specific Energy, U_{nc}

$$U_{nc} = \frac{P_c}{MRR}$$

- Spindle Specific Energy, U_s

$$U_s = \frac{P_s}{MRR}$$

- Machine Specific Energy, U_m

$$U_m = \frac{P_m}{MRR}$$

Where P_c , P_s , and P_m are the cutting power, spindle power, and machine power respectively.

3.3.1 Comparison of Flood and Dry Milling

Each test was performed 7 times in order to average the results and reduce error. The first case entailed measuring the energy consumption of milling SLMed IN718 with coolant. Figure 3.2 shows the results of this test, displaying spindle energy and power as a function of time.

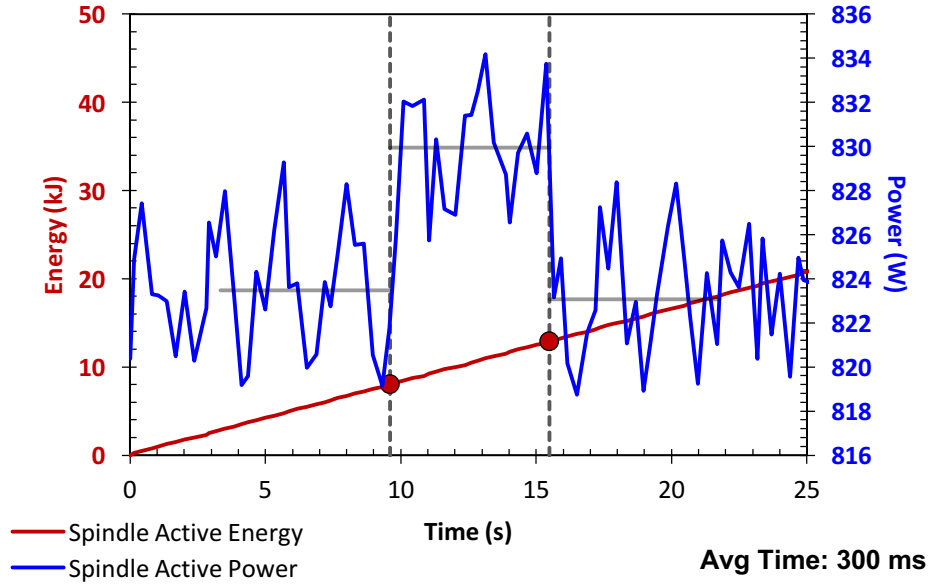


Figure 3.2 Spindle Energy and Power Consumption in Flood Milling of SLMed IN718

In this figure, the blue line displays the power consumed by the spindle and the red line displays the spindle energy consumption. The vertical dashed lines represent the starting and ending points of the cutting pass. This shows that the jump in average power is due to the cutting load. As previously mentioned, the net cutting specific energy was found by dividing the net cutting power by the material removal rate [35]. In this case, the average net cutting power was found to be 6.46 W and the material removal rate was 1.19 mm³/s, resulting in a net cutting specific energy (U_{nc}) of 5.41 J/mm³. The specific energy from the spindle (U_s) was defined similarly by dividing the spindle power by the material removal rate to be 696.32 J/mm³. Finally, the total specific energy consumption (U_m) was found to be 1664.87 J/mm³.

The first step in analyzing this data is to compare it to the dry-machined counterpart, shown in Figure 3.3. When comparing the two images, the first aspect to note is the highly similar values for the average non-cutting and cutting spindle power usage, depicted by the horizontal gray bars in the images. While an increase in total power usage is expected when flood machining due to the use of the pump, the spindle power usage remains relatively stable. This is because, once all of the other auxiliary energy uses have been removed, all that remains is the energy required to rotate the spindle and the energy required to cut the material. This is why the spindle energy also only differs slightly between cases. The specific cutting energy is an extremely small component of the overall energy usage, as most of the energy consumed by the machine is for auxiliary functions.

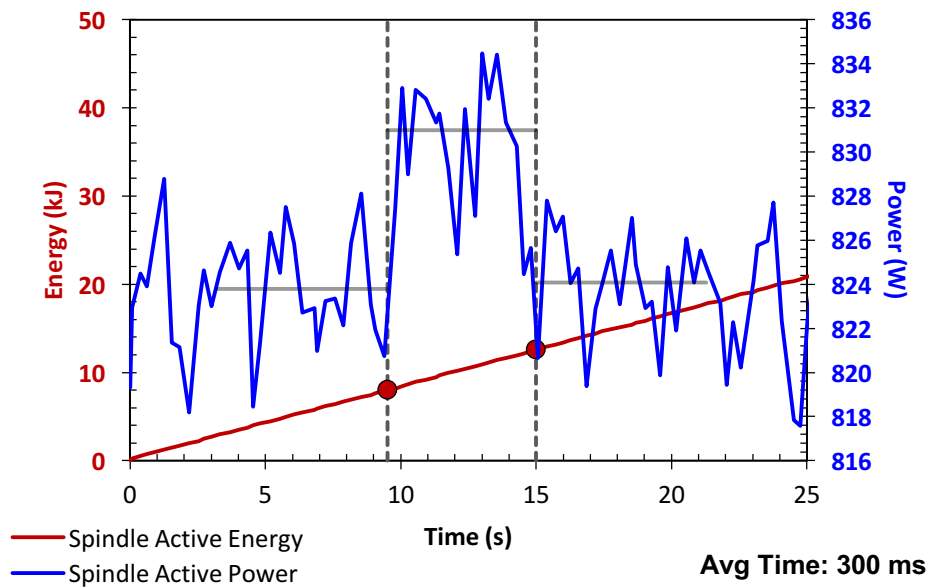


Figure 3.3 Spindle Energy and Power Consumption in Dry Milling of SLMed IN718

When comparing flood and dry machining, there are two mechanisms that dominate the net cutting specific energy. The first is the tendency for a part to heat up and soften under dry

machining due to the friction. As the part softens, it becomes easier to mill and the net cutting specific energy decreases as a result. The second mechanism is in regards to flood machining, and represents the opposite viewpoint. The coolant serves to decrease the coefficient of friction between the tool and the part, also serving to decrease the net cutting specific energy. The lower specific cutting energy depends on which mechanism dominates the relationship, and must be tested for each material. The average specific cutting energy, specific spindle energy consumption, and total specific energy consumption for both the flood-machined case and dry-machined case are shown in Table 3.1. The data is presented in the following manner: (Average Value, Standard Deviation)

Table 3.1 Energy Data of SLMed Samples

Milling Type	U_{nc} (J/mm ³)	U_s (J/mm ³)	U_m (J/mm ³)
Flood	(5.41, 0.47)	(696.32, 1.75)	(1664.87, 4.72)
Dry	(5.73, 0.30)	(696.24, 1.10)	(1467.03, 3.90)

Comparing the specific cutting energy shows that lowering the coefficient of friction with coolant is more important in terms of machinability than the softening effect seen in dry machining. The use of coolant decreases the specific cutting energy by 0.32 J/mm³, or 5.6%. The spindle power remains relatively constant which is expected, with a percent difference of only 0.011%. The machine specific energy consumption increased by 198 J/mm³, or 13.5%, with the

use of coolant. As mentioned before, this increase is due to the use of the pump required for the coolant flow. These values changes show that coolant use increases the overall machinability of the samples, however this benefit is outweighed by the increased energy requirement of the pump.

3.3.2 Comparison of Milling Conventional and SLMed IN718

3.3.2.1 Flood-Milling

The conventionally manufactured IN718 was milled with identical process parameters to the SLMed samples. Figure 3.4 shows the spindle energy and power consumption in the flood milling of conventional IN718.

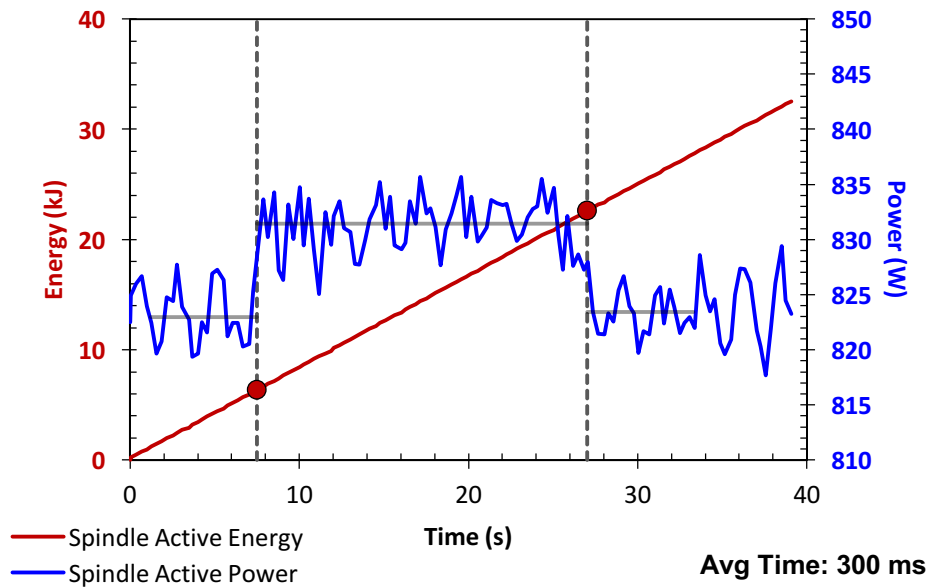


Figure 3.4 Spindle Energy and Power Consumption in Flood Milling of Traditional IN718

When comparing the slope of Figure 3.4 to Figure 3.2, it is seen that they are nearly identical (0.83 kJ/s for both). This means that the overall spindle energy consumption rate remained identical and lends credence to the accuracy and repeatability of the overall test.

Additionally, the average cutting and non-cutting spindle power remained constant as well. The difference in the two tests arises when comparing the average specific cutting energy, specific spindle energy consumption, and total specific energy consumption as shown in Table 3.2.

Table 3.2 Energy Data of Flood Milling SLMed and Traditional IN718

Sample Type	U_{nc} (J/mm ³)	U_s (J/mm ³)	U_m (J/mm ³)
SLM	(5.41, 0.47)	(696.32, 1.75)	(1664.87, 4.72)
Conventional	(6.93, 0.01)	(697.08, 0.77)	(1656.36, 2.88)

Table 3.2 shows that the net cutting specific energy in flood-milling of IN718 increases by 1.52 J/mm³, or 28%. Additionally, the standard deviation of the SLMed samples is significantly higher than the conventional samples. These are both sizable increases, and are most likely due to the porosity (Figure 3.5) induced in SLM. Additionally, the standard deviation of the SLMed samples is significantly higher than the conventional samples. These porosities can occur from a multitude of reasons, such as a thick powder layer, defects like the balling effect, imperfect laser power and scan speed, and scanning strategy of the laser. In the cross-section shown below, an example of the balling effect can be seen at the top of the left side void. This effect has been shown by Kruth et. al. to be mitigated through optimization of laser power and scan speed, however this is a process that needs to be tested for each material used [12]. As expected, the spindle and machine specific energy remain stable. This again shows the

repeatability of the test. Since cutting energy is such a small component of the overall machine's energy consumption, any changes in U_{nc} will only slightly affect U_s and U_m .



Figure 3.5 Porosity in SLM produced Samples

3.3.2.2 Dry-Milling

After analyzing the data comparing the flood-machined samples, the assumption was made that conventionally manufactured IN718 would have a higher specific cutting energy under dry-milling conditions as well. The spindle energy and power consumption for this test is shown in Figure 3.6.

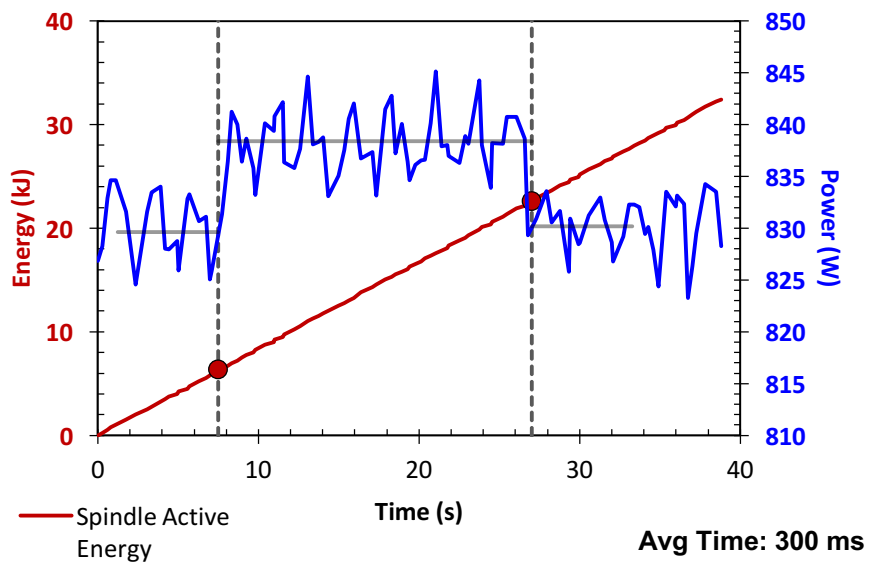


Figure 3.6. Spindle Energy and Power Consumption in Dry Milling of Traditional IN718

The energy consumption rate of the spindle again stayed constant, however the spindle power usage was slightly higher in the traditional IN718 in both the cutting and non-cutting phases. This increase is relatively small overall, with an average percent difference of only 0.78%. The average net cutting specific energy, spindle specific energy, and machine specific energy for this test is shown in Table 3.3.

Table 3.3 Energy Data of Dry Milling SLMed and Traditional IN718

Sample Type	U_{nc} (J/mm ³)	U_s (J/mm ³)	U_M (J/mm ³)
SLM	(5.73, 0.30)	(696.24, 1.10)	(1467.03, 4.72)
Conventional	(7.27, 0.53)	(700.67, 1.67)	(1482.19, 3.43)

The data found in the dry-milling comparison is similar to that of the flood-milling comparison. The spindle specific energy consumption and machine specific energy consumption again stayed constant for the most part, with percent differences of only 0.64% and 0.86% respectively. The specific cutting energy increased significantly when machining the conventionally manufactured IN718 compared to the SLMed sample. It was expected that the percent difference in the flood and dry milling cases would be similar, and this was found to be true. The overall increase was 1.54 J/mm^3 , and a percent increase of 27%. In both cases, the specific cutting energy increased by about 1.5 J/mm^3 when machining the conventional part.

3.4 Summary

It is evident that the energy consumption is highly influenced by the porosity and microstructure in the SLMed parts. When comparing the net cutting specific energy under both conditions (flood and dry), the energy usage to mill traditionally manufactured Inconel 718 is significantly higher than that of the SLMed IN718. In order to further test and compare these two production techniques for IN718, the SLM process must be improved and optimized in order to minimize the porosities. Once the parts reach near-full density, a more effective comparison regarding the influence of microstructure can be made as to any differences in cutting energy required.

The additional finding was that, as expected, the decreased friction as a result of the use of coolant played a larger role in decreasing the net cutting specific energy than the softening effect as a result of heat created from dry machining. The future research may evaluate the use of coolant to see if there are any changes in performance of a part as a result of the coolant choice,

and if the energy trade off could be justified by the additional pump during flood machining and the decreased frictional coefficient.

CHAPTER 4

SUMMARY AND FUTURE OUTLOOK

The first step to continuing this work is to further optimize the process parameters used to make the parts. This needs to be done since voids and porosities play such a large role in part performance and especially hardness. Since this single factor dominates the overall hardness of the part, it is difficult to quantify any improvement that machining has on a part due to measurement fluctuations caused by porosity. Once the near full density part is produced, a nano-indenter may be used to effectively quantify the change in hardness in the near subsurface (the upper 40 microns closest to the surface). This would make it easy to quantify the exact effect that machining has on hardness in the part, and whether or not the use of coolant has any effect.

Additionally, the microstructure should be more closely analyzed in order to see if the fluctuations in hardness are truly due to porosities, or if certain phases (such as γ'') are the cause of certain low hardness zones. The specific areas for analysis are the outlier shown in Figure 2.17 and the part-substrate interface.

As for energy usage, the next step would be to transcribe the entire conventional and additive processes into specific energy in order to compare the overall energy consumption. This would include the embodied energy in the parts themselves, as well as factors such as tool wear. The creation of such a model would allow effective comparisons to be made on the the overall sustainability of each process and would assist in choosing the optimal process for individual needs.

Next, the end performance of a SLMed material should be tested with and without a machining step in order to quantify any changes in final functionality. These tests would include experiments on fatigue, wear, and corrosion resistance. It is the author's expectation that the use of machining would improve each of the performance factors, however the question is to what degree.

Lastly, the immediate future study is to continue Brinksmeier's work in order to find the process space to maximize the effects of machining.

REFERENCES

- [1] Kruth J-, Leu MC, Nakagawa T. Progress in additive manufacturing and rapid prototyping. *CIRP Ann Manuf Technol.* 1998;47(2):525-540.
- [2] Levy GN, Schindel R, Kruth JP. Rapid Manufacturing and Rapid Tooling with Layer Manufacturing (LM) Technologies, State of the Art and Future Perspectives. *CIRP Ann Manuf Technol.* 2003;52(2):589-609.
- [3] Gong X, Anderson T, Chou K. Review on powder-based electron beam additive manufacturing technology. *Proceedings of the ASME/ISCIE 2012 International Symposium on Flexible Automation.* 2012.
- [4] Fu CH, Guo YB. Three-dimensional temperature gradient mechanism in selective laser melting of ti-6Al-4V. *J. Manuf. Sci. Eng.* 2014;136(6).
- [5] Murr LE, Martinez E, Gaytan SM, et al. Microstructural architecture, microstructures, and mechanical properties for a nickel-base superalloy fabricated by electron beam melting. *Metallurgical and Materials Transactions.* 2011;42(11):3491-3508.
- [6] Shin K, Natu H, Dutta D, Mazumder J. A method for the design and fabrication of heterogeneous objects. *Mater Des.* 2003;24(5):339-353.
- [7] Frazier WE. Metal additive manufacturing: A review. *Journal of Materials Engineering and Performance.* 2014;23(6):1917-1928.
- [8] Laser metal deposition. <http://www.xsecpro.biz/laser-metal-deposition>. Updated 2014. Accessed January 1, 2017.
- [9] Christensen A. Additive manufacturing in metal: New option for medical applications. *MoldMaking Technology.* 2007;9/30/2016.
- [10] Hiemenz J. Additive manufacturing trends in aerospace: Leading the way. *Stratasys: For a 3D World.* 2013;9/30/2016.
- [11] Kellner T. The FAA cleared the first 3D printed part to fly in a commercial jet engine from GE. <http://www.gereports.com/post/116402870270/the-faa-cleared-the-first-3d-printed-part-to-fly/>. Updated 2015. Accessed January 19, 2017.

- [12] Kruth JP, Froyen L, Van Vaerenbergh J, Mercelis P, Rombouts M, Lauwers B. Selective laser melting of iron-based powder. *J Mater Process Technol.* 2004;149(1–3):616-622.
- [13] Zaeh MF, Branner G. Investigations on residual stresses and deformations in selective laser melting. - *Production Engineering*. 2010(4 - 1):- 35.
- [14] Bremen S, Meiners W, Diatlov A. Selective laser melting. *Laser Technik Journal.* 2012;9(2):33-38.
- [15] Prem F, Leordean D, Balc N, Pacurar R. The influence of working parameters of SLM technology on surface quality and precision of stainless steel parts. *Annals of MTM for 2011 & Proceedings of the 10th International MTM Conference*, Napoca, Romania. 2011.
- [16] Kelly SM, Kampe SL. Microstructural evolution in laser-deposited multilayer ti-6Al-4V builds: Part II. thermal modeling. *Metallurgical and Materials Transactions.* 2004;35(6):1869-1879.
- [17] Lewis GK, Schlienger E. Practical considerations and capabilities for laser assisted direct metal deposition. *Mater Des.* 2000;21(4):417-423.
- [18] Li R, Shi Y, Wang Z, Wang L, Liu J, Jiang W. Densification behavior of gas and water atomized 316L stainless steel powder during selective laser melting. *Appl Surf Sci.* 2010;256(13):4350-4356.
- [19] Kirchner A, Kloden B, Weissgarber T, et al. Mechanical properties of ti-6Al-4V additively manufactured by electron beam melting. *Euro PM2015*, Politecnico di Torino, Italy. 2015.
- [20] Tolochko NK, Mozzharov SE, Yadroitsev IA, et al. Balling processes during selective laser treatment of powders. *Rapid Prototyping Journal.* 2004;10(2):78-87.
- [21] Mercelis P, Kruth J. Residual stresses in selective laser sintering and selective laser melting. *Rapid Prototyping Journal.* 2006;12(5):254-265.
- [22] Kruth J, Mercelis P, Van Vaerenbergh J, Froyen L, Rombouts M. Binding mechanisms in selective laser sintering and selective laser melting. *Rapid Prototyping Journal.* 2005;11(1):26-36.
- [23] Brandl E, Heckenberger U, Holzinger V, Buchbinder D. Additive manufactured AlSi10Mg samples using selective laser melting (SLM): Microstructure, high cycle fatigue, and fracture behavior. *Materials and Design.* 2012;34:159-169.
- [24] Kumar S, Kruth JP. Wear performance of SLS/SLM materials. *Advanced Engineering Materials.* 2008;10(8):750-753.
- [25] Lucca DA, Brinksmeier E, Goch G. Progress in assessing surface and subsurface integrity. *CIRP Ann Manuf Technol.* 1998;47(2):669-693.

- [26] Brinksmeier E, Levy G, Meyer D, Spierings AB. Surface integrity of selective-laser-melted components. *CIRP Ann Manuf Technol.* 2010;59(1):601-606.
- [27] Kempen, K., Thijs, L., Yasa, E., & Kruth, J. P. (2011). Process optimization and microstructural analysis for selective laser melting of AlSi10Mg. *Solid Freeform Fabrication Symposium*, Texas, USA., 22.
- [28] Li, C., Guo, Y. B., & Zhao, J. B. (2017). Interfacial phenomena and characteristics between the deposited material and substrate in selective laser melting inconel 625. *Journal of Materials Processing Technology*, 243, 269-281.
- [29] Li, W. (2013). The Fundamental Relationship Among Tool Wear, Surface Integrity, and Fatigue in Milling of Difficult-to-cut Alloys.
- [30] Chatterjee, A. N., Kumar, S., Saha, P., Mishra, P. K., & Choudhury, A. R. (2003). An experimental design approach to selective laser sintering of low carbon steel. *Journal of Materials Processing Technology*, 136(1–3), 151-157.
- [31] *Sustainable manufacturing*. Retrieved April 01, 2017, from <https://archive.epa.gov/sustainablemanufacturing/web/html/>
- [32] Zhai, Q. (2012). *Recycling metal chips from manufacturing industry through a combined hydrodynamic and electromagnetic separation approach*. WI, USA: University of Wisconsin - Milwaukee.
- [33] Harman, A. (2009). *Forecast predicts commodities to rebound in second-half 2009*. Retrieved April 01, 2017, from <http://wardsauto.com/news-analysis/forecast-predicts-commodities-rebound-second-half-2009>
- [34] Henriquez, V. (2009). *China drives 1.8% increase in global copper consumption in 2009 - WBMS*. Retrieved April 01, 2017, from http://www.bnamicas.com/news/metals/China_drives_1,8*_increase_in_global_copper_consumption_in_2009_-_WBMS
- [35] Z.Y. Liu, M.P. Sealy, Y.B. Guo, Z.Q. Liu, 2015, “Energy consumption characteristics in finish hard milling of tool steels”, *Procedia Manuf.*, 1, 477-486.